

The role of transition, intermittency and phase interference in airfoil secondary tones

Tulio R. Ricciardi¹, William R. Wolf^{1†} and Kunihiro Taira²

¹School of Mechanical Engineering, University of Campinas, Campinas, SP 13083-860, Brazil

²Department of Mechanical and Aerospace Engineering, University of California, Los Angeles, CA 90095, USA

(Received xx; revised xx; accepted xx)

A wall-resolved large eddy simulation is performed to study secondary tones generated by a NACA0012 airfoil at $\alpha = 3^\circ$ with freestream Mach number $M_\infty = 0.3$ and Reynolds number $Re = 5 \times 10^4$. Laminar separation bubbles are observed over the suction side and near the trailing edge on the pressure side. Flow visualization and spectral analysis are employed to investigate vortex shedding aft of the suction side separation bubble. Vortex interaction results in merging or bursting such that coherent structures or turbulent packets are advected towards the trailing edge leading to different levels of noise emission. Despite the intermittent occurrence of laminar-turbulent transition, the noise spectrum depicts a main tone with multiple equidistant secondary tones. To understand the role of flow instabilities on the tones, the linearized Navier-Stokes equations are examined in its operator form through bi-global stability and resolvent analyses, and by time evolution of disturbances using a matrix-free method. These linear global analyses reveal amplification of disturbances over the suction side separation bubble. Non-normality of the linear operator leads to further transient amplification due to modal interaction among eigenvectors. Two-point correlations of pressure along the spanwise direction elucidate aspects of the acoustic feedback loop mechanism in both the linear and non-linear solutions. This feedback process is self-sustained by acoustic waves radiated from the trailing edge, which reach the most sensitive flow location between 10 and 18% of the airfoil chord as identified by the resolvent analysis.

1. Introduction

Trailing-edge noise is an overriding concern for design of quiet air vehicles. At low and moderate Reynolds numbers, tonal noise becomes an important component of the acoustic spectrum. Several studies on trailing-edge aeroacoustics were conducted starting in the 1970s to examine the tonal noise generation by airfoils (Paterson *et al.* 1973; Tam 1974; Fink 1975; Longhouse 1977; Arbey & Bataille 1983). Paterson *et al.* (1973) performed noise measurements for symmetric NACA airfoils over a Reynolds number range between 10^5 and 10^6 at various angles of attack. Their results showed the existence of multiple tones in a ladder-like structure in terms of frequency and freestream velocity. These authors also found strong two-point correlation of surface pressure along the spanwise direction. This indicated that the flow phenomenon associated with tonal noise generation could be modeled as two-dimensional.

Tam (1974) suggested that the ladder-like structure is due to a self-excited feedback loop between disturbances in the boundary layer and the airfoil wake. Fink (1975) assumed that the discrete tonal frequencies are related to the laminar boundary layer on

† Email address for correspondence: wolf@fem.unicamp.br

the pressure side. In order to elucidate aspects of airfoil noise, Arbey & Bataille (1983) performed experiments in an open wind tunnel for different NACA airfoils at $\alpha = 0^\circ$ for $1 \times 10^5 \leq Re \leq 7 \times 10^5$. The aforementioned studies showed that the noise spectrum has a broadband component with a main tonal peak plus a set of equidistant secondary tones due to a feedback mechanism closing at the point of maximum flow velocity along the airfoil. The broadband component was assumed to appear due to scattering of Tollmien-Schlichting (TS) instabilities. For airfoils at incidence, Lowson *et al.* (1994) found that the presence of secondary tones was related to a separation bubble developed on the airfoil pressure side. In this case, TS instabilities developing along the laminar boundary layer would lead to acoustic scattering on the trailing edge and acoustic waves would then propagate upstream closing the feedback loop, with the separation bubble acting as an amplifier of acoustic disturbances.

Nash *et al.* (1999) performed experimental studies of airfoil noise for a NACA0012 profile up to a Reynolds number of 1.45×10^6 and several angles of attack. A closed-section wind tunnel, with and without acoustic-absorbing lining on its walls, was used in the experiments and results from the hard-wall tunnel revealed multiple frequency peaks. However, the authors argued that these tonal peaks were correlated to resonant frequencies of the wind tunnel. Thus, they carried out measurements with lined walls simulating anechoic conditions and a single dominant tone was observed instead of several peaks. Furthermore, no ladder-like structure of tonal frequency was observed, in disagreement with previous studies of Paterson *et al.* (1973), Fink (1975) and Arbey & Bataille (1983). It is important to mention that secondary tones were often observed in experiments conducted in open-jet facilities. More recently, Plogmann *et al.* (2013) also found multiple tones in their experiments (NACA0012, $3.1 \times 10^5 \leq Re \leq 1.5 \times 10^6$, $0^\circ \leq \alpha \leq 9^\circ$) and demonstrated that tripping the pressure side boundary layer leads to turbulent flow, eliminating the separation bubble and the secondary tones. These authors emphasize that the feedback loop is extremely sensitive to small changes in the flow conditions what, in turn, lead to changes in the tonal components.

Two-dimensional flows were investigated by Desquesnes *et al.* (2007) who conducted direct numerical simulations of a NACA0012 airfoil for a Reynolds number $Re = 1 \times 10^5$ at an angle of attack $\alpha = 2^\circ$, and for $Re = 2 \times 10^5$ at $\alpha = 5^\circ$. These authors observed multiple tonal peaks consistent with experimental observations from Arbey & Bataille (1983). They also performed 1D local stability analysis and showed that the main tone frequency radiated to the far-field was close to that most amplified along the pressure side boundary layer. Desquesnes *et al.* (2007) also discussed the amplitude modulation of velocity fluctuations computed near the trailing edge. It was assumed that such modulation is caused by interference of vortical structures from both sides of the airfoil which, combined with the feedback loop mechanism, would lead to the presence of multiple tones.

Following the work of Desquesnes *et al.* (2007), Pröbsting *et al.* (2014) employed particle image velocimetry for flows at Reynolds numbers $1 \times 10^5 \leq Re \leq 2.7 \times 10^5$ and $2^\circ \leq \alpha \leq 4^\circ$. They investigated the mechanisms associated with tonal noise generation and the interference effects between suction and pressure sides of the airfoil. For $Re = 1.5 \times 10^5$, at the lowest angle of attack, the authors showed that the amplitude modulation discussed by Desquesnes *et al.* (2007) was related to phase interference of boundary layer instabilities occurring on both sides of the trailing edge.

As discussed above, experiments report the presence of a separation bubble on the airfoil pressure side. Most of these investigations were conducted at higher Reynolds numbers, where the flow was likely turbulent on the suction side. These observations are in agreement with the large eddy simulations of a NACA0012 at $\alpha = 5^\circ$ and $Re = 4 \times 10^5$

performed by Wolf *et al.* (2012a) and Ricciardi *et al.* (2019). Flow visualization and proper orthogonal decomposition were used in these references to identify coherent structures shed from the pressure side near the trailing edge. Such flow structures were found responsible for the intense tonal noise generation despite the fact that a turbulent boundary layer developed on the airfoil suction side. In this case, the pressure side boundary layer was laminar due to the favorable pressure gradient. When both boundary layers were tripped, Wolf *et al.* (2012a) showed that the tonal component vanished.

Angle of attack and Reynolds number dependencies on tonal noise emission are highlighted by Pröbsting *et al.* (2015). These authors performed experiments for $0.3 \times 10^5 \leq Re \leq 2.3 \times 10^5$ and effective angles of attack $0^\circ \leq \alpha \leq 6.3^\circ$ for a NACA0012 airfoil profile. To understand the role of such interactions, tripping was applied on both sides of the airfoil separately. They discuss that tonal noise generation is dominated by suction-side (pressure-side) events at lower (higher) Reynolds numbers. Moreover, it was found that, at low angles of attack, interactions between the two sides of the airfoil become increasingly important.

Direct numerical simulations were performed by Jones *et al.* (2008) for a NACA0012 airfoil at a moderate Reynolds number $Re = 5 \times 10^4$, $M_\infty = 0.4$ and $\alpha = 5^\circ$. These authors investigated the impact of a laminar separation bubble (LSB) on the airfoil suction side. It was shown that, despite being absolutely stable by means of linear stability analysis, turbulence is self-sustained even with the absence of forcing. Later, experimental work by Pröbsting & Yarusevych (2015) with a NACA0012 airfoil at moderate Reynolds numbers $0.65 \times 10^5 \leq Re \leq 4.5 \times 10^5$ and $\alpha = 2^\circ$ presents intermittent laminar-turbulent transition that affects the advection of coherent structures from the LSB towards the trailing edge. Further analyses were also presented by Kurelek *et al.* (2016, 2018, 2019) and Michelis *et al.* (2018) for $Re_c \approx 1 \times 10^5$ at an incidence of 4° . These authors studied the impact of acoustic excitation, three-dimensional effects and shedding/merging of vortices on the dynamics of the suction side LSB. Sanjose *et al.* (2019) employed different modal decomposition techniques to relate the vortices shed from the LSB to the tonal noise components for an airfoil at $Re = 1.5 \times 10^5$. The authors found that intermittency played a key role in the flow dynamics and noise emission for the configuration investigated.

Fosas de Pando *et al.* (2014a,b, 2017) applied bi-global stability and resolvent analyses to study the dynamics of wavepackets driving the feedback loop mechanism in a 2D flow over a NACA0012 airfoil for $Re = 2 \times 10^5$, $M_\infty = 0.4$ and $\alpha = 2^\circ$. These authors found multiple frequencies in the eigenspectrum related not only to the main tonal peak but also to the secondary tones. Before this work, the stability analyses were conducted in a local sense, i.e. by means of 1D profiles, and only a discussion of the dominant tonal frequency was presented. Considering 2D flows, Ricciardi *et al.* (2020) studied a NACA0012 at $Re = 1.0 \times 10^5$ and showed that the multiple tones are related to modulation of the TS waves on the suction side. In this case, the instantaneous main frequency alternates in time due to phase modulation of the vortical structures shed by the LSB. As a consequence, multiple equidistant frequencies must appear in the Fourier transform to reconstruct the modulated signals. Several numerical models discussed in the literature on the mechanisms of secondary tones in airfoils are two-dimensional. However, the flow features in laminar 2D simulations must be carefully interpreted since the vorticity dynamics is different from that of more realistic 3D flows. In 2D models, vortex stretching is absent and inverse kinetic energy cascade may be present through merging of small-scale into large-scale vortices (Boffetta & Ecke 2012).

In the present work, wall-resolved large eddy simulation (LES) is performed to study secondary tones and the acoustic feedback mechanism. Hence, flow features previously

neglected in 2D studies can be accounted for, including vortex stretching and transition to turbulence. The problem setup analyzed is a NACA0012 airfoil at $\alpha = 3^\circ$ immersed in a freestream flow with Mach number $M_\infty = 0.3$ and Reynolds number $Re = 5 \times 10^4$. Details on the numerical methods are presented in Section 2. Laminar separation bubbles are observed over the suction side and near the trailing edge on the pressure side in terms of mean flow, as presented in Section 3.1. Flow visualization is employed in Section 3.2 to investigate vortex shedding aft of the suction side separation bubble. Vortex interaction results in merging or bursting such that coherent structures or turbulent packets are advected towards the trailing edge leading to different levels of noise emission. Despite the intermittent occurrence of laminar-turbulent transition, spectral analysis in Section 3.3 presents the frequency spectrum with multiple equidistant secondary tones. To understand the role of flow instabilities on these secondary tones, in Section 3.4 the linearized Navier-Stokes equations are examined in its operator form using bi-global stability and resolvent analyses, and by time evolution of disturbances using a matrix-free method. Finally, in Section 3.5 two-point spanwise pressure correlations elucidate aspects of the acoustic feedback loop mechanism in both the linear and non-linear solutions. The intermittent transition is analyzed in terms of amplitude and phase interference between the frequency of hydrodynamic disturbances.

2. Theoretical and Numerical Approaches

2.1. Large eddy simulation

A large eddy simulation is performed to solve the compressible Navier-Stokes equations in general curvilinear coordinates. The spatial discretization of the governing equations employs a sixth-order accurate compact scheme for derivatives and interpolations on a staggered grid (Nagarajan *et al.* 2003). The time integration is carried out by a hybrid method. The implicit second-order scheme of Beam & Warming (1978) is applied in the near-wall region to overcome the stiffness problem due to a fine boundary layer grid, while a third-order Runge-Kutta scheme is used for time advancement of the equations in flow regions away from the solid boundary. For the communication across the different methods, information is exchanged at overlapping points. Outside the boundary layer, a sixth-order compact filter (Lele 1992) is applied to control high-wavenumber numerical instabilities arising from grid stretching and interpolation between staggered grids. An explicit sub-grid scale model is not applied; however, the transfer function associated with such filters has been shown to provide an approximation to sub-grid scale models (Mathew *et al.* 2003).

No-slip adiabatic wall boundary conditions are enforced along the airfoil surface and characteristic plus sponge boundary conditions are applied in the far-field locations to minimize wave reflections. Periodic boundary conditions are used in the spanwise direction. Length scales, velocity components, density, pressure and temperature are non-dimensionalized as $\mathbf{x} = \mathbf{x}^*/L^*$, $\mathbf{u} = \mathbf{u}^*/a_\infty^*$, $\rho = \rho^*/\rho_\infty^*$, $p = p^*/\rho_\infty^* a_\infty^{*2}$ and $T = T^*/[(\gamma - 1)T_\infty^*]$, respectively. Here, L^* is the airfoil chord, a_∞^* is the freestream speed of sound, ρ_∞^* is the freestream density, T_∞^* is the freestream temperature and γ is the ratio of specific heats. Quantities with superscript $*$ are given in dimensional units. Herein, time and frequency (Strouhal number) are presented non-dimensionalized by freestream velocity as $t = t^* U_\infty^*/L^*$ and $St = f^* L^*/U_\infty^*$, respectively. The numerical approach has been extensively validated for several 2D and 3D simulations of compressible flows around airfoils (Wolf *et al.* 2012a,b, 2013; Ricciardi *et al.* 2019; Ramos *et al.* 2019).

The computational O-grid employed for the LES is shown in gray lines for every 3

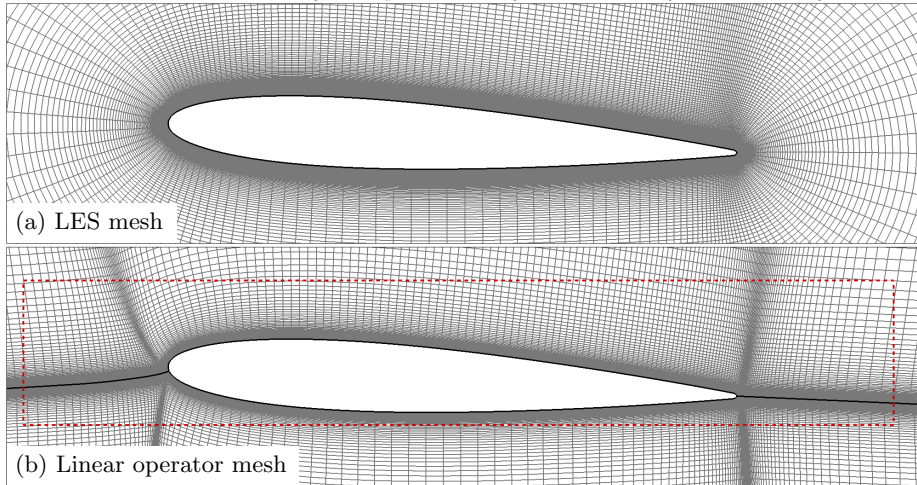


FIGURE 1. Computational grids near the airfoil for both (a) LES and (b) linear analysis shown skipping every 3 points. Sub-figure (a) shows the 3D O-mesh with 76×10^6 grid points and 317×10^3 points per plane. Sub-figure (b) shows the 2D H-mesh with 520×10^3 grid points.

points in figure 1(a). For a smooth O-grid generation, the original airfoil trailing edge is truncated at 98% of the chord and it has a curvature radius $r/L^* = 0.4\%$. The reference length scale L^* is the unit chord from the original NACA0012 airfoil. The leading edge is placed at $(x, y) = (0, 0)$ such that the airfoil is pivoted about this point. The total wingspan has $0.4L^*$, being larger compared to previously reported studies of airfoil flows for this range of Reynolds number (Jones *et al.* 2008; Ducoin *et al.* 2016). The domain extends 37 chord-lengths outwards with a sponge occupying the last 10 chord lengths. The ratio of grid points along the suction side relative to the pressure side is approximately 5:3. The mesh has a distribution of points in the streamwise, wall-normal and spanwise directions given by $n_x = 660$, $n_y = 600$ and $n_z = 192$, respectively, which results in approximately 76×10^6 grid points. The wall-normal distance of the first grid point is $\Delta n = 0.0001$ and the stretching ratio is 1.5%. This grid resolution showed convergence of results in terms of mean and fluctuation properties for 2D simulations (Ricciardi *et al.* 2021). However, in the present simulation, the flow is three-dimensional and it transitions to turbulence. Considering only the turbulent flow region on the suction side, near the trailing edge, the estimated mesh resolution in terms of wall units is given by $\Delta x^+ < 10$, $\Delta y^+ \approx 0.3$ and $\Delta z^+ < 5$. These results guarantee adequate resolution of the present LES. The time step is $\Delta t = 1.5 \times 10^{-4}$ and 75 convective time units are employed for post-processing and analysis of results. The 3D simulation starts from a 2D flow superposed with random noise and more than 30 convective time units are discarded before collecting statistics.

2.2. Linear stability and resolvent analyses

Through a Reynolds decomposition, it is possible to split the unsteady flow in a mean base flow $\bar{\mathbf{q}}(\mathbf{x})$ plus a time-dependent fluctuation component $\mathbf{q}'(\mathbf{x}, t)$. If the fluctuations are sufficiently small, it is possible to linearize the Navier-Stokes equations about the (mean) base flow. Although it is possible to consider the turbulent mean flow $\bar{\mathbf{q}}$ as the base flow, the linear stability analysis would not hold because such state is not an equilibrium point of the NS equations. However, the use of a time-averaged base flow may provide some insights as a model (Taira *et al.* 2017, 2020). With addition of a time-dependent

external forcing $\mathbf{f}'(\mathbf{x}, t)$, the linearized Navier-Stokes equations (LNS) can be written as

$$\frac{\partial \mathbf{q}'}{\partial t} = \mathcal{L}\mathbf{q}' + \mathcal{B}\mathbf{f}' , \quad (2.1)$$

where $\mathcal{B} = \mathcal{B}(\mathbf{x})$ is an operator which serves as a spatial window where forcing is applied. The matrix $\mathcal{L} = \mathcal{L}(\bar{\mathbf{q}})$ is the bi-global LNS operator with the spanwise time-averaged flow properties $\bar{\mathbf{q}}(\mathbf{x})$ as base flow.

The evolution of linear disturbances by equation 2.1 can be performed by a direct analysis of the operator \mathcal{L} or time-integrating the disturbances in a linearized version of the CFD code. In the former case, with a transformation

$$\bullet'(x, y, z, t) = \int_{-\infty}^{\infty} \int_{-\infty}^{\infty} \hat{\bullet}(x, y, \beta, \omega) e^{i(\beta z - \omega t)} d\beta d\omega , \quad (2.2)$$

where the wavenumber $\beta \in \mathbb{R}$ and the frequency $\omega \in \mathbb{C}$, it is possible to write the forced LNS equations in discrete form as

$$-i\omega \hat{\mathbf{q}} = \mathbf{L}\hat{\mathbf{q}} + \mathbf{B}\hat{\mathbf{f}} . \quad (2.3)$$

In this case, the linear operator becomes a function of the spanwise wavenumber $\mathbf{L} = \mathbf{L}(\bar{\mathbf{q}}, \beta)$ and \mathbf{B} is the discrete version of \mathcal{B} . If forcing $\hat{\mathbf{f}}$ is absent, the LNS equations can be analyzed separately for each wavenumber β as an eigenvalue problem (linear stability analysis) as

$$\mathbf{Q}\mathbf{\Lambda} = \mathbf{L}\mathbf{Q} . \quad (2.4)$$

Here, \mathbf{Q} holds the eigenvectors of \mathbf{L} and the eigenvalues appear in the diagonal matrix $\mathbf{\Lambda} = -i\omega\mathbf{I}$, where the frequency and growth rate are the real and imaginary parts of ω , respectively. Due to the velocity gradients appearing off-diagonal, the linear operator becomes a non-normal matrix such that $\mathbf{L}^*\mathbf{L} \neq \mathbf{L}\mathbf{L}^*$. As a consequence, the eigenvectors are non-normal.

The sensitivity region of the flow is analyzed by the eigenvalue decomposition of the adjoint operator $\mathbf{L}^{\mathcal{H}}$

$$\mathbf{Q}^{\dagger}\mathbf{\Lambda}^{\mathcal{H}} = \mathbf{L}^{\mathcal{H}}\mathbf{Q}^{\dagger} . \quad (2.5)$$

In this equation, the superscript \mathcal{H} denotes the complex conjugate transpose (Hermitian). The eigenvalues of the adjoint operator are the complex conjugate of those from direct analysis. The eigenvectors \mathbf{Q}^{\dagger} represent the region of flow sensitivity and they are equal to \mathbf{Q}^{-1} for normal systems. On the other hand, this is not true for non-normal systems. A thorough review on the significance of adjoint operators is presented by Luchini & Bottaro (2014) and references therein.

In case forcing is applied at a frequency $\tilde{\omega}$, equation 2.1 yields

$$\hat{\mathbf{q}} = (-i\tilde{\omega}\mathbf{I} - \mathbf{L})^{-1}\mathbf{B}\hat{\mathbf{f}} = \mathbf{H}\mathbf{B}\hat{\mathbf{f}} , \quad (2.6)$$

where the matrix $\mathbf{H} = \mathbf{H}(\bar{\mathbf{q}}, \beta, \tilde{\omega})$ is the resolvent operator (Reddy & Henningson 1993; Schmid 2007; McKeon & Sharma 2010; Taira *et al.* 2017, 2020).

For non-normal operators, eigenvalue sensitivity and energy amplification are related to the induced L_2 norm of operator \mathbf{H} , *i.e.*, the leading singular value σ obtained from singular value decomposition

$$\mathbf{H} = \mathbf{U}\mathbf{\Sigma}\mathbf{V}^* . \quad (2.7)$$

In this equation, \mathbf{V} and \mathbf{U} are unitary matrices holding right and left singular vectors and $\mathbf{\Sigma}$ is a diagonal matrix containing the singular values σ , such that

$$\|\mathbf{H}\| = \max(\sigma) . \quad (2.8)$$

The first column of \mathbf{V} contains the forcing term that produces the largest response in the flow (first column in matrix \mathbf{U}) with the amplification ratio given by Σ .

A variable transformation using a matrix \mathbf{W} is applied to convert variables $\hat{\mathbf{q}}$ and $\hat{\mathbf{f}}$ with an appropriate energy norm prior to performing the SVD. In the case of compressible flows, the Chu norm which relates density, velocity and temperature (Chu 1965) is typically used. A spatial window $\mathbf{C} = \mathbf{C}(\mathbf{x})$ is applied to limit the spatial domain of analysis and the system response in Fourier domain $\hat{\mathbf{y}}$ is given by

$$\hat{\mathbf{y}} = \mathbf{WC}\hat{\mathbf{q}}. \quad (2.9)$$

Combining equations 2.6 and 2.9 leads to the modified resolvent operator

$$\mathbf{H}_w = \mathbf{WC}(-i\tilde{\omega}\mathbf{I} - \mathbf{L})^{-1}\mathbf{BW}^{-1}. \quad (2.10)$$

The amplification mechanisms of flow disturbances can be identified by using the eigenvalue decomposition of the linearized NS operator, equation 2.4, in the resolvent, yielding

$$\mathbf{H}_w = \mathbf{WC}(-i\tilde{\omega}\mathbf{I} - \mathbf{Q}\mathbf{\Lambda}\mathbf{Q}^{-1})^{-1}\mathbf{BW}^{-1} = \mathbf{WCQ}(-i\tilde{\omega}\mathbf{I} - \mathbf{\Lambda})^{-1}\mathbf{Q}^{-1}\mathbf{BW}^{-1}, \quad (2.11)$$

where $\mathbf{\Lambda}$ and \mathbf{Q} are the eigenvalues and eigenvectors from the solution of equation 2.4. The bounds of the resolvent-induced L_2 norm are

$$\left\| (-i\tilde{\omega}\mathbf{I} - \mathbf{\Lambda})^{-1} \right\| \leq \left\| \mathbf{H}_w \right\| \leq \left\| (-i\tilde{\omega}\mathbf{I} - \mathbf{\Lambda})^{-1} \right\| \left\| \mathbf{Q} \right\| \left\| \mathbf{Q}^{-1} \right\|, \quad (2.12)$$

where the lower bound is the case of an operator with orthonormal eigenvectors. In this case, the norm depends only of the resonance, following a $1/R$ decay based on the distance R in complex plane with respect to the eigenvalues. For non-normal systems, the norm also depends on the pseudoresonance, measured by the product of eigenvectors \mathbf{Q} and their inverse \mathbf{Q}^{-1} . The weighting \mathbf{W} and the two windowing matrices \mathbf{B} and \mathbf{C} are included in the norm calculation (see Schmid & Henningson (2001); Symon *et al.* (2018) for more details).

To perform the global stability (spectral) and resolvent (pseudospectral) analyses, the discrete linear operator is computed using the second-order accurate methodology from Sun *et al.* (2017) and Yeh & Taira (2019). The base flow is the time-spanwise averaged solution from the LES, $\bar{\mathbf{q}} = [\bar{\rho}, \bar{u}, \bar{v}, \bar{w}, \bar{T}]$. For the far-field boundary and airfoil surface, Dirichlet boundary conditions are set for $[\rho', u', v', w'] = [0, 0, 0, 0]$ and a Neumann boundary condition is set for T' such that the wall-normal derivative $\partial T' / \partial n = 0$. At the outlet boundary, the same Neumann boundary condition is set for all flow variables. With these boundary conditions and the mean base flow $\bar{\mathbf{q}}$, the linear operator is computed in its discrete form $L(\bar{\mathbf{q}}, \beta)$ for a prescribed spanwise wavenumber β .

The mean flow $\bar{\mathbf{q}}$ obtained is interpolated from the O-grid in figure 1(a) to the H-mesh shown in figure 1(b) for the modal analysis. This is necessary to improve spatial accuracy of the linear operator downstream and upstream of the airfoil, where direct and adjoint eigenvectors are supported, respectively (Yeh & Taira 2019). The present two-dimensional H-mesh has an extent of $x \in [-5, +7]$, $y \in [-5, +5]$ and it is composed of approximately 520×10^3 grid points. The mesh refinement targets a Strouhal number cut-off $St = 8.0$. The sponge region comprises a circle with parabolic growth $f = a(r - r_0)^2$ for $r > r_0$. The sponge is centered at $(x, y) = (0.5, 0)$ with $a = 1.0$ and $r_0 = 1.5$. The mesh refinement and sponge placement are assessed by convergence of physically meaningful eigenvalues while suppressing spurious eigenvalues. If the mesh is coarse or the sponge is placed too far from the airfoil, it was observed that the meaningful eigenvectors also exhibit spatial support in the same region of the spurious eigenvectors.

For the pseudospectrum calculation, the dashed red rectangle in figure 1(b) depicts

the region considered for the present resolvent analysis in terms of operators \mathbf{B} and \mathbf{C} in equation 2.10. This windowing is important not only from a physical point of view, where the noise sources close to the airfoil surface are most important, but it also enables the removal of spurious eigenvectors, which are mostly observed far away from the body. Finally, the SVD in equation 2.10 is performed with the randomized algorithm presented by Ribeiro *et al.* (2020).

2.3. Mean flow perturbation

The properties of the resolvent operator can be studied as an initial value problem, although these approaches are not trivially related, as described by McKeon & Sharma (2010). Due to the non-normality, large transient energy amplification can be observed even in stable problems (Trefethen *et al.* 1993). The time evolution of perturbations with respect to the mean flow can be performed with a linearized version of the CFD code according to equation 2.1. However, here we employ an approach that uses the present LES code with the addition of a force term to the right-hand side of the equations (Touber & Sandham 2009; Bhaumik *et al.* 2015). In this approach, known as mean flow perturbation, the Reynolds decomposition $\mathbf{q} = \bar{\mathbf{q}} + \mathbf{q}'$ is applied to the non-linear NS equations which are expressed as

$$\frac{\partial(\bar{\mathbf{q}} + \mathbf{q}')}{\partial t} = \mathcal{N}(\bar{\mathbf{q}} + \mathbf{q}') . \quad (2.13)$$

The turbulent mean flow $\bar{\mathbf{q}}$ is not an equilibrium state of the NS equations and its time derivative $\partial_t \bar{\mathbf{q}}$ is non-null. Hence, in order to use it as a base flow, an additional term \mathcal{R} must be added in the numerical procedure to keep the base flow stationary. A Taylor series expansion about the base state $\bar{\mathbf{q}}$ yields

$$\frac{\partial(\bar{\mathbf{q}} + \mathbf{q}')}{\partial t} = \mathcal{N}(\bar{\mathbf{q}} + \mathbf{q}') = \mathcal{N}(\bar{\mathbf{q}}) + \frac{\partial \mathcal{N}(\bar{\mathbf{q}})}{\partial \mathbf{q}} \mathbf{q}' + \frac{1}{2} \frac{\partial^2 \mathcal{N}(\bar{\mathbf{q}})}{\partial^2 \mathbf{q}} \mathbf{q}'^2 + \dots + \mathcal{R} . \quad (2.14)$$

Grouping together the base flow terms results in

$$\frac{\partial \mathbf{q}'}{\partial t} + \left(\frac{\partial \bar{\mathbf{q}}}{\partial t} - \mathcal{N}(\bar{\mathbf{q}}) - \mathcal{R} \right) = \frac{\partial \mathcal{N}(\bar{\mathbf{q}})}{\partial \mathbf{q}} \mathbf{q}' + \frac{1}{2} \frac{\partial^2 \mathcal{N}(\bar{\mathbf{q}})}{\partial^2 \mathbf{q}} \mathbf{q}'^2 + \dots , \quad (2.15)$$

where the base flow is stationary when

$$\left(\frac{\partial \bar{\mathbf{q}}}{\partial t} - \mathcal{N}(\bar{\mathbf{q}}) - \mathcal{R} \right) = 0 . \quad (2.16)$$

Considering that the imposed perturbation amplitude \mathbf{q}' is sufficiently small leads to a linearized solution of the NS equations as

$$\frac{\partial \mathbf{q}'}{\partial t} \approx \frac{\partial \mathcal{N}(\bar{\mathbf{q}})}{\partial \mathbf{q}} \mathbf{q}' = \mathbf{L} \mathbf{q}' , \quad (2.17)$$

where the Jacobian $\frac{\partial \mathcal{N}(\bar{\mathbf{q}})}{\partial \mathbf{q}}$ is the linearized operator \mathbf{L} . Details on the implementation can be found in Ranjan *et al.* (2018). In contrast to the previous approach in section 2.2, this methodology is matrix-free and the linear operator is never explicitly computed. Despite this, the method still accounts for the modal interaction that leads to transient energy amplification within a non-normal analysis of the linear operator.

The system response is obtained by the time evolution of the disturbances and the initial condition is set as an impulsive excitation that triggers the dominant response. In the current analysis, the grid and numerical methodology employed are the same used in the LES.

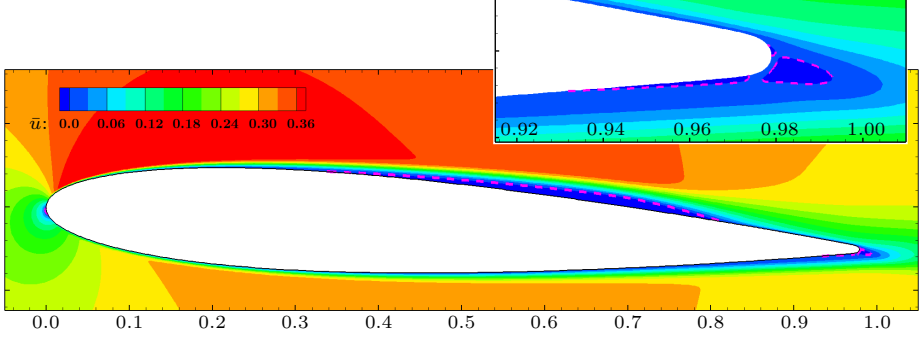


FIGURE 2. Contours of mean streamwise velocity \bar{u} normalized by freestream speed of sound. The magenta dashed line depicts the reversed flow boundaries which include a wide separation bubble on the suction side besides a small bubble on the pressure side, near the trailing edge.

3. Results

The physical mechanisms responsible for generation of secondary tones in airfoil flows are investigated by post-processing the non-linear results from LES and also employing linear stability theory. The linear analysis provides insights on the onset and growth of disturbances in the flow besides its receptivity. On the other hand, LES results allow the investigation of transition, intermittency and phase interference effects in the context of the multiple secondary tones and acoustic feedback.

3.1. Mean flow

The mean flow is presented with contours of u -velocity normalized by the freestream speed of sound in figure 2. Important flow features can be observed including a long recirculation bubble that extends over the suction side, from the detachment at $x = 0.34$ until its reattachment at $x = 0.82$. In the magnified view, a small bubble can be observed on the pressure side, followed by a recirculation region at the trailing edge. The regions enclosed by magenta lines indicate locations of reversed flow.

Values of root-mean-square (RMS) for kinetic energy k and pressure p are presented in figures 3(a) and (b), respectively. As it can be seen from the plots, fluctuations start amplifying along the bubble and the highest values appear at the reattachment region, on the suction side. Strong velocity and pressure fluctuations are observed along the trailing edge region. The green and blue dashed lines in figures 3(a) and (b), respectively, depict the locations of maximum k and p along the shear layer forming on the suction side. In the following analyses, these lines will be used to track flow disturbances as reference location for data extraction. The solid magenta line shows the recirculation bubble.

The negative mean pressure coefficient $-C_p$ is shown in figure 4(a) with blue and red solid lines for suction and pressure sides, respectively. To highlight the regions with intense fluctuations, the pressure coefficient is presented as $-C_p \mp C_{p_{RMS}}$, where the blue dashed and red dotted lines correspond to the suction and pressure sides, respectively. The peak value of pressure coefficient on the suction side is observed near the leading edge at $x = 0.02$. From this point, a pressure increase leads to a drop in $-C_p$ until reaching a plateau along the laminar separation bubble. The plateau extends up to $x = 0.7$, where the pressure further increases towards the trailing edge, causing another drop in $-C_p$. Pressure fluctuations can be observed in figure 4(d) for both the suction and pressure sides. The RMS values of C_p are low along the entire pressure side, and upstream the bubble ($x < 0.5$) on the suction side. However, they increase towards the peak at $x \approx 0.78$ on the suction side, as shown in the figure.

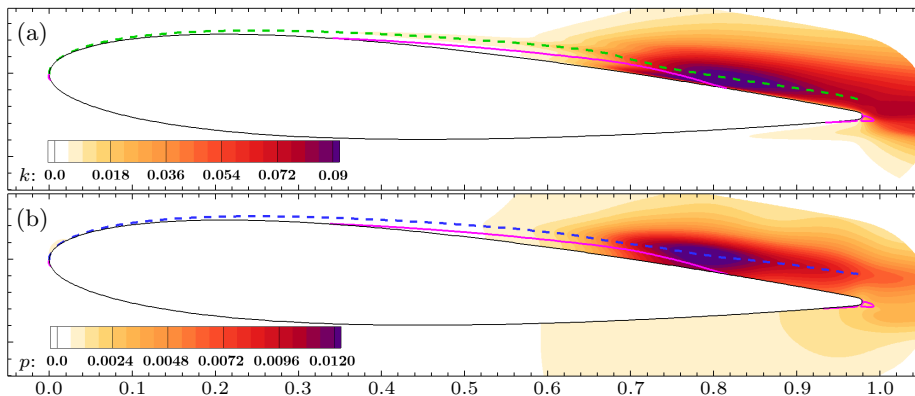


FIGURE 3. RMS values of (a) kinetic energy and (b) pressure. The green and blue dashed lines depict locations of maximum fluctuations along the shear layer on the suction side, while the magenta solid line delimits the reversed flow region.

The mean skin friction distribution over the airfoil C_f is presented in figure 4(b). The RMS values of skin friction $C_{f_{\text{RMS}}}$, shown in figure 4(e), are also added to the mean values. A magnified view highlights the presence of the laminar separation bubble which starts at $x = 0.34$ and reattaches at $x = 0.67$. The reattachment is followed by a second detachment which reaches a minimum at $x = 0.75$ and reattaches at $x = 0.82$. The RMS peaks at $x \approx 0.76$ due to the high value of k shown in figure 3(a).

Mean tangential velocity profiles extracted along the wall normal direction Δn are presented in figure 4(c) at different locations along the chord. At the detachment point, $x = 0.34$, the red curve shows inflection in the velocity profile. At $x = 0.73$, the velocity profile shown as a grey line exhibits the maximum reversed flow of $-0.13U_\infty$. The orange line shows a velocity profile at $x = 0.95$, where three-dimensional effects are important due to turbulent transition. In figure 4(f), RMS values of the tangential velocity are presented and a single peak is observed for the profile computed at $x = 0.34$. Velocity fluctuations increase inside the bubble at $x = 0.64$ and become dominant at $x = 0.73$. In both these locations, the velocity fluctuations present triple peak profiles as also observed by Nash *et al.* (1999), Desquesnes *et al.* (2007) and Duck *et al.* (2000). Near the trailing edge at $x = 0.95$, where a turbulent regime may occur, mixing results in a smoother velocity fluctuation profile.

3.2. Vortex dynamics

Instantaneous three-dimensional flow fields over the airfoil are presented in figure 5 with iso-surfaces of Q -criterion colored by u -velocity. A magenta shade along the airfoil surface depicts the region of reversed flow along the separation bubble. This figure shows two-dimensional rolls that are visible along the separation bubble and amplify on the suction side, leading to vortex shedding and intermittent turbulent transition. Different flow regimes are observed at the trailing edge, where high spanwise coherence alternates with periods of turbulent packets. For example, figure 5(a) shows a single spanwise correlated roll reaching the trailing edge at $t = 20.82$ while figure 5(b) shows that, at $t = 21.78$, vortex breakdown leads to a turbulent regime near the trailing edge. Readers are referred to the movie of the flow field provided as supplemental material (movie 1) for detailed inspection of the present flow dynamics.

The normalized two-point correlation of pressure fluctuations is computed along the spanwise direction Δz at each time t . Calculations are performed near the trailing edge

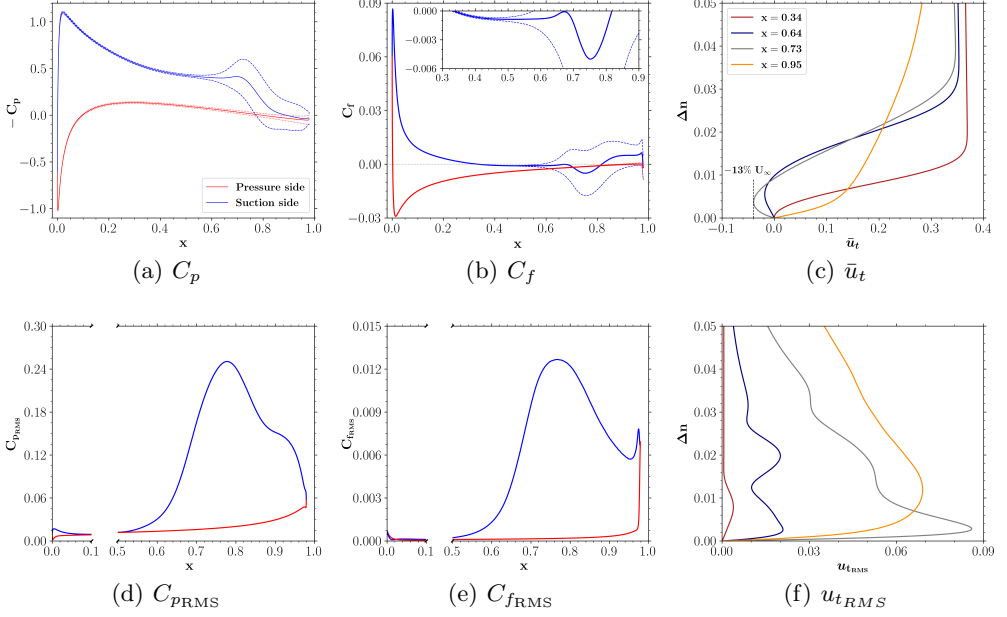


FIGURE 4. Mean and RMS distributions of pressure and friction coefficients along the airfoil surface, and tangential velocity profiles computed in the wall-normal direction Δn .

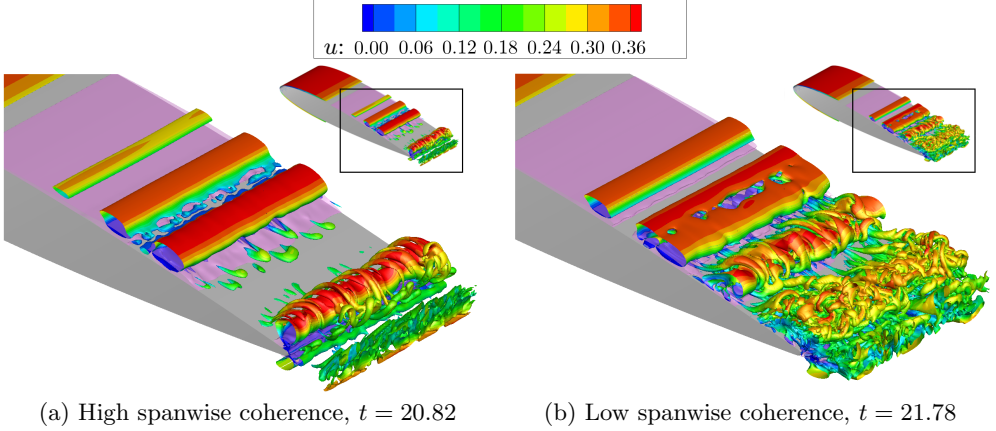


FIGURE 5. Instantaneous iso-surfaces of Q-criterion colored by u -velocity illustrating regimes (a) with coherent structures at the trailing edge and (b) with smaller-scale turbulent eddies.

at $x = 0.98$ and results are presented in figure 6. The dark lines display higher spanwise correlation which are related to the two-dimensional vortex rolls illustrated in figure 5(a). These coherent structures generate noise very efficiently upon reaching the trailing edge as shown in figure 7(a). On the other hand, uncorrelated turbulence is related to the white regions in the plot which radiate sound with less intensity, as can be seen in figure 7(b). The frequency in which the major coherent structures are advected past the trailing edge are related to a period of $\Delta t = 2.0$ convective time units. However, it is possible that multiple vortices reach the trailing edge within this period as indicated by the time differences $\Delta t = 0.22, 0.25, 0.29, 0.33$ and 0.40 in the figure.

When the vortices arrive at the trailing edge, acoustic waves are emitted with intensities

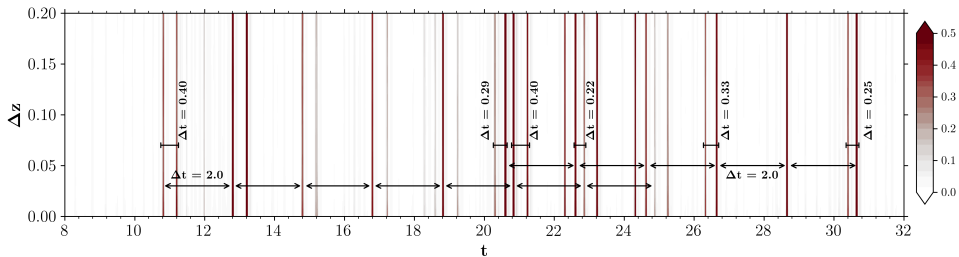


FIGURE 6. Two-point pressure correlation along the spanwise direction (Δz) as a function of time (t) at the trailing edge. High correlation repeats about every 2 convective time units with intermittent events in between.

that are related to their hydrodynamic coherence. Such waves are scattered with a π phase opposition relative to the incident fluctuations. Instantaneous hydrodynamic pressure fluctuations p'_h are presented in figures 7(a,c) with black-white contours, while the acoustic fluctuations p'_a are presented in figures 7(b,d) with levels which are 10 times lower compared to their equivalent hydrodynamic ones. The figures also display ω_z vorticity in red-blue colors. To highlight the spanwise coherence, regions of $|\omega_z| > 24$ are plotted as filled contours. The vortex cores are related to lower pressures (white background contours) while the gaps between the cores display higher pressures (black contours). A coherent vortex at the trailing edge is presented in figure 7(a) at a time instant $t = 20.82$. The highly coherent hydrodynamic structure leads to a more efficient acoustic scattering at the trailing edge which, in turn, induces the emission of an intense acoustic wave that reaches the leading edge at a retarded time $t = 21.31$, as shown in figure 7(b). When the flow is turbulent, at $t = 21.78$, a less coherent vorticity packet reaches the trailing edge as shown in figure 7(c). In this case, a weaker acoustic wave is emitted from the trailing edge, reaching the leading edge at a retarded time of $t = 22.27$, as exhibited in figure 7(d). A movie of figure 7 is submitted as supplemental material (movie 2) to show the relation between the acoustic field and vortex dynamics.

The analysis of flow snapshots is important to understand the overall vorticity dynamics over the airfoil suction side. Since the pressure correlation analysis confirms the presence of spanwise coherent structures, the analysis of 2D averaged properties will be employed to filter the influence of uncorrelated three-dimensional effects. Figure 8 shows the spanwise averaged ω_z vorticity with an interval of $\Delta t = 0.12$ convective time units. Blue and red contours represent negative and positive z -vorticity, respectively. A dark blue color indicates strong spanwise coherence of a 2D vortex, while light blue contours are representative of uncorrelated turbulence. A thin black line is used to identify individual vorticity packets, based on the iso-contour of an entropy measure given by $p/\rho^\gamma = 0.715$. This separates the region where vorticity is important from where the flow is irrotational, outside the boundary layer. A magenta dashed line represents the border of averaged negative \bar{u} velocity, as discussed in figure 2. The simulation time is shown in convective time units on the lower left corner of all plots. A movie of figure 8 is provided as supplemental material (movie 3) to aid the dynamic visualization of the flow features.

As shown in figure 8, the flow dynamics is dominated by events on the suction side, where TS instability waves are shed from the laminar separation bubble. During the shedding process, there is a possibility that the 2D laminar vortices undergo a process of vortex pairing. If the merging is not successful, vortex bursting leads to turbulent transition and low coherence along the span, represented by dotted lines. These turbulent packets may interact with other vortices and further reduce their coherence, as indicated by the dashed-dotted line. On the other hand, if the vortices merge or only a solitary

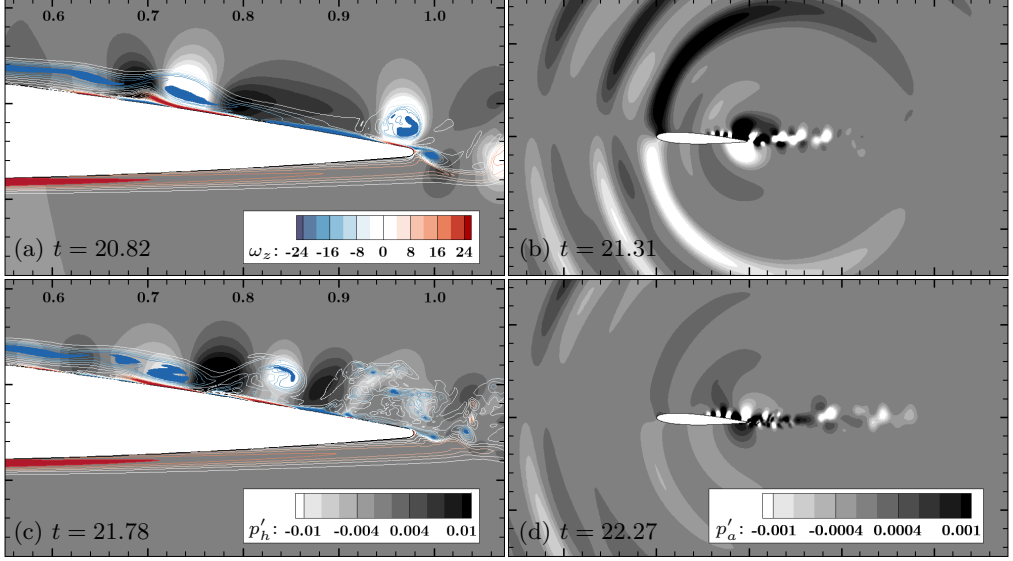


FIGURE 7. Acoustic radiation from the airfoil. Sub-figure (a) shows a coherent structure near the trailing edge at $t = 20.82$ and its subsequent intense acoustic wave reaching the leading edge in sub-figure (b), at a retarded time $t = 21.31$. Sub-figure (c) shows an uncorrelated turbulent packet near the trailing edge at $t = 21.78$ and its subsequent weaker acoustic wave reaching the leading edge in sub-figure (d), at a retarded time $t = 22.27$. The acoustic levels p'_a from figures (b,d) are 10 times lower than the hydrodynamic ones p'_h from figures (a,c).

vortex is shed from the bubble, the trend is for either structure to keep its high coherence up to the trailing edge. Both of these processes are represented by the solid and dashed lines in figure 8, which coincide with the high correlation values shown in figure 6. Similar dynamics of vortex shedding from LSB are observed experimentally by Kurelek *et al.* (2016).

It is important to mention that, for this Reynolds number and angle of attack, the pressure side does not show any relevant dynamics. In this case, vortices are shed at the trailing edge due to conservation of circulation during the passage of suction side structures. The overall dynamics discussed here has similarities to case 3 from Pröbsting *et al.* (2014) (at $Re = 1.3 \times 10^5$), where the flow is laminar on the pressure side until the trailing edge and large scale turbulent packets are observed on the suction side.

Inside the region of reversed mean flow (magenta dashed line), it is possible to see small packets of high positive values of ω_z near the wall. This is due to the induced velocity by the large-scale vortices that induce shearing of the flow against the wall. With the vortex rotation, the positive vorticity is ejected from the wall and leads to flow reattachment. This induces high values of kinetic energy fluctuation inside the recirculation bubble, previously described in figure 3(a). Downstream from the bubble and away from the wall, the kinetic energy is dominated by motion of large-scale structures. In terms of pressure fluctuation, the dark purple region in figure 3(b) marks the position of pairing and merging of the low pressure vortex cores. The vorticity dynamics also impacts both pressure and friction coefficients shown in figure 4. The fluctuations of C_p and C_f are low up to $x = 0.5$, where non-linear effects are still negligible. Then, the growth and saturation of instabilities increase unsteadiness, peaking before $x = 0.8$, where the vortex merging process is complete. In this interval, the shear of positive vorticity induced by

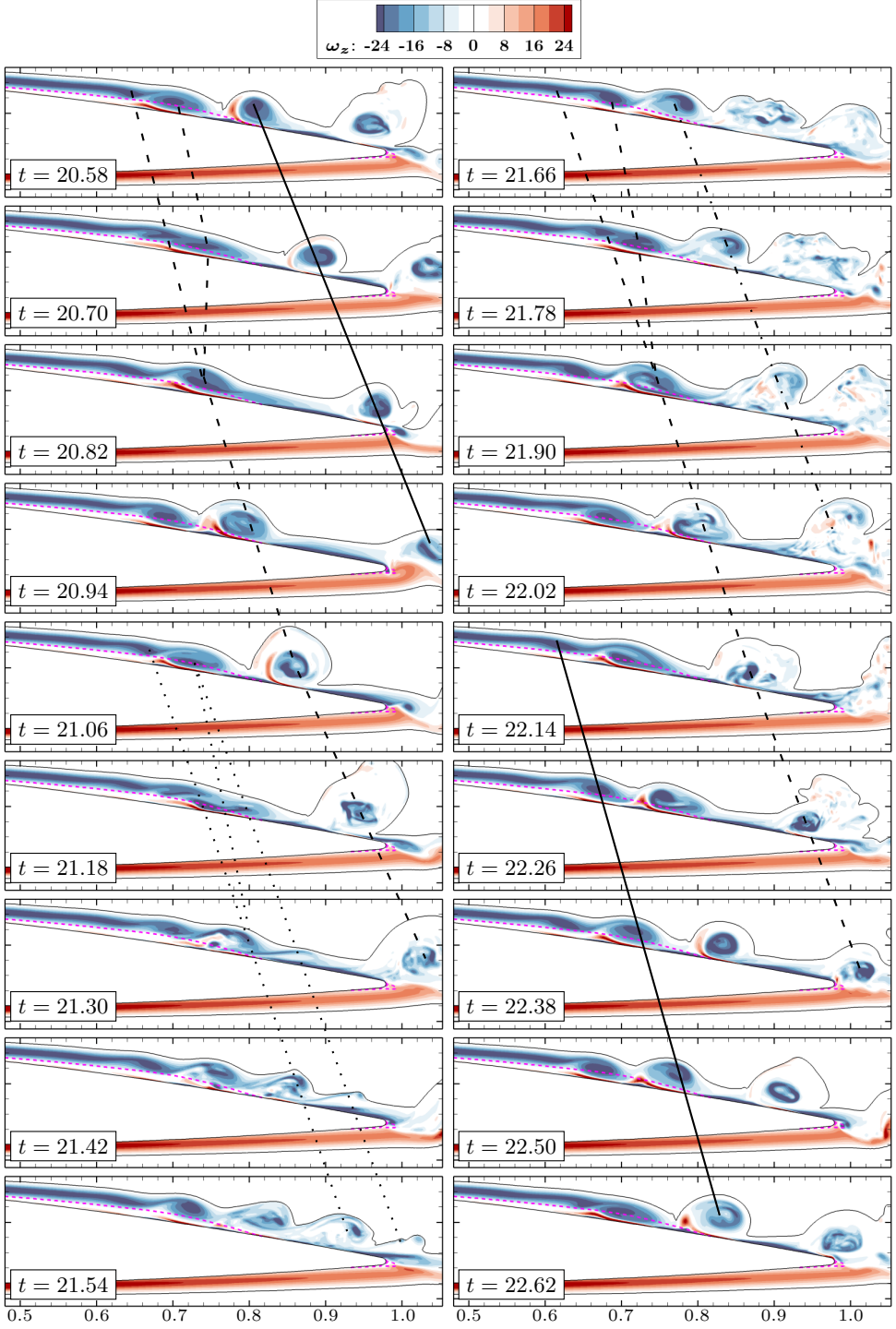


FIGURE 8. Spanwise averaged vorticity ω_z shows vortex pairing over the airfoil. The magenta dashed line represents the boundary of reversed flow (negative \bar{u}). The black lines mark the evolution of vortices with high (— and ---) or low (··· and - · -) coherence.

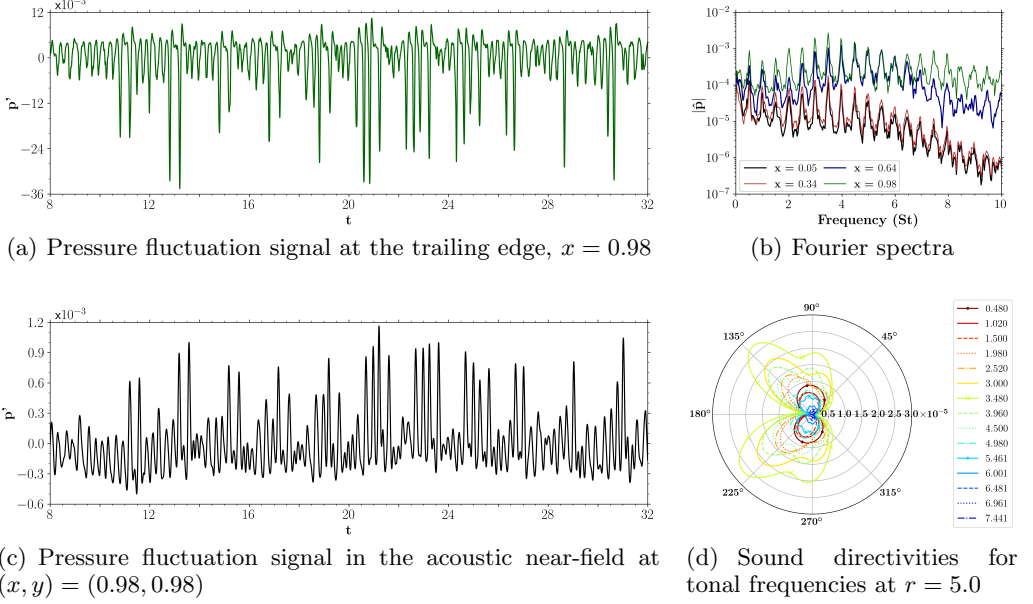


FIGURE 9. Spectral analysis of spanwise averaged pressure at different locations inside the boundary layer along the chord (Fourier spectrum) and in the acoustic field (directivity).

the large vortices dominates the behavior of skin friction. For pressure, the merging of vortex cores affects this coefficient more than the dynamics on the wall.

3.3. Spectral analysis

For the spectral analysis, temporal signals are acquired at different positions along the blue dashed line in figure 3(b) in terms of spanwise averaged pressure. The signal at the trailing edge is presented in figure 9(a) and displays intermittent deep valleys related to the passage of coherent structures as shown in figure 7(a). The signal also shows low amplitude oscillations related to the turbulent packets that carry a negative pressure envelope, as described in figure 7(b). The Fourier transforms of the hydrodynamic pressure signals are presented in figure 9(b), displaying equidistant multiple tones. The transformation employs Welch's method with an overlap of 67% amongst 4 bins covering the entire period, the frequency resolution is $\Delta f = 0.03$ and a Hanning window function with energy correction is applied. All tonal peaks are integer multiples of the lowest frequency tone, $St \approx 0.5$. As can be seen from the figure, the dominant peak is 7 times the lowest frequency $St \approx 3.5$ for probes located upstream of the recirculation bubble ($x = 0.05$), at the detachment point ($x = 0.34$) and the trailing edge ($x = 0.98$). This frequency is related to the passage of low pressure packets, either turbulent or coherent. At $x = 0.64$, in the shear-layer roll-up region, the dominant peak moves to a higher frequency, at $St \approx 4.5$, and this may be related to the smaller scale instabilities yet to be merged into larger vortices.

The acoustic pressure signal is extracted one chord above the trailing edge, at $(x, y) = (0.98, 0.98)$, and it is presented in figure 9(c). It is possible to see that the low pressure valleys from figure 9(a) result in high pressure peaks that reach the observer position at a retarded time. The spectral analysis is shown in figure 9(d) in terms of sound directivities for each one of the tones from the Fourier spectrum. The directivities are computed directly by LES at a distance of $r = 5$ chords from the trailing edge, without

the use of acoustic analogy. At low frequencies, $St \leq 1.50$, the noise is a vertically oriented dipole and, as the frequency increases, the directivity tends to a cardioid shape. However, a perfect cardioid is not observed due to the secondary diffraction effects from the finite chord. All these trends in terms of noise emission are discussed by Wolf *et al.* (2012a). In agreement with pressure data at the trailing edge, the sound radiation is more intense at $St = 3.48$.

Destructive and constructive interference of vortical structures during the pairing and merging process can be interpreted as an amplitude modulation of the signal (Desquesnes *et al.* 2007; Ricciardi *et al.* 2020). The modulation mechanism from the 2D simulations performed in these references differs from the current 3D case, where turbulent transition occurs. The destructive interference leads to vortex breakdown and smaller pressure fluctuations. On the other hand, constructive interference of multiple frequencies creates spikes in the pressure signal which leads to a behavior similar to that observed in a Dirac comb function, as shown for certain time instants in figures 9(a) and (c).

A time-frequency analysis is also performed and results are presented in figure 10. The top row shows the continuous wavelet transform using the complex Morlet wavelet (Farge 1992). This function is the product of a monochromatic complex exponential with a Gaussian envelope. Its spectral response is an exponentially decaying pass-band filter centered around the frequency of the complex exponential. The filter width depends on the Gaussian standard deviation. The scalogram presents how the correlation of the wavelet with a reference signal changes in time based on the wavelet frequency. Hence, higher values indicate strong fluctuations of the signal at a particular frequency and time. Results are obtained for the same probe locations considered in figure 9(b). The scalograms from figures 10(a) and (c) exhibit longer periods of intense pressure fluctuations at $St \approx 3.5$, while in figure 10(b), a broader range of frequencies is excited more intensely. As can be seen from the probe at $x = 0.64$, frequencies higher than $St \approx 3.5$ are excited with a particular temporal dominance of $St \approx 4.5$. One should note that the color levels are different for each location, with lower and higher amplitudes for probes at $x = 0.34$ and 0.98 , respectively. These figures show that the secondary tones present intermittent behavior, with each frequency experiencing periods of silence (blue contours) and loud noise emission (green, yellow and red contours).

The bottom row shows the normalized two-point pressure correlation along the span, computed for each time step over the entire simulation period. The values are normalized with respect to the maximum at each location for a qualitative analysis and are not intended for comparison amongst different probe locations. It is possible to see that the dark lines in the correlation plots are associated to the excitation of the secondary tones in the wavelet scalogram. This indicates that specific frequencies are related to quasi 2D flow structures. Furthermore, as it can be seen from figure 6, coherent structures often reach the trailing edge with a period of $\Delta t \approx 2.0$, which corresponds to a frequency $St \approx 0.5$. However, due to the chaotic motion, this process is not perfectly periodic and multiple vortices may reach the trailing edge within this period. This is highlighted in figure 6, where different time intervals between vortex pairs with $\Delta t \approx 0.22, 0.25, 0.29, 0.33$ and 0.40 are related to frequencies $St \approx 4.5, 4.0, 3.5, 3.0$ and 2.5 , respectively. All these frequencies are integer multiples of the low frequency tone at $St \approx 0.5$. Hence, if successive coherent structures reach the trailing edge, not only the instantaneous magnitude of the wavelet transform increases but it is possible that the dominant frequency changes.

In order to investigate the growth of velocity and pressure fluctuations at the main tonal frequencies, figure 11 presents Fourier transforms of the temporal signals extracted along the airfoil suction side, following the green (velocities) and blue (pressure) dashed lines from figures 3(a) and (b), respectively. In this analysis, the temporal signals are

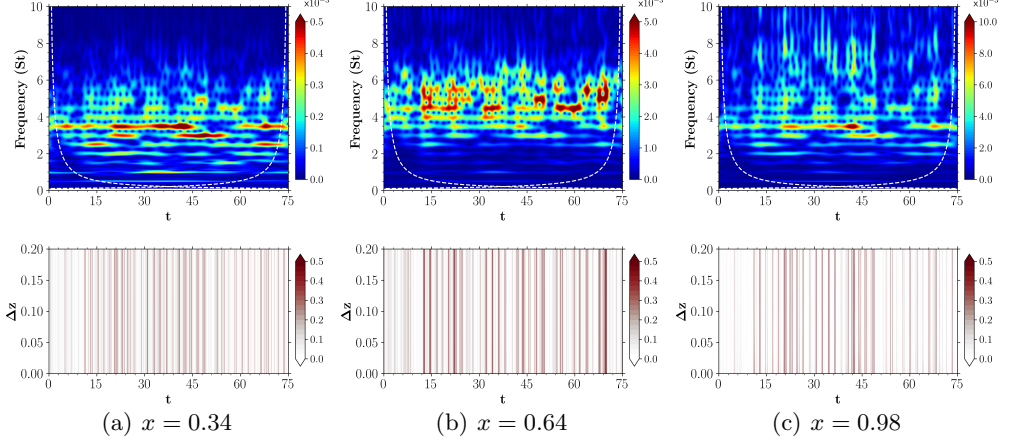


FIGURE 10. Time-frequency analysis of pressure fluctuations using a continuous wavelet transform (top) and spanwise two-point correlations (bottom) at (a) the detachment point $x = 0.34$, (b) shear-layer roll-up $x = 0.64$ and (c) trailing edge $x = 0.98$.

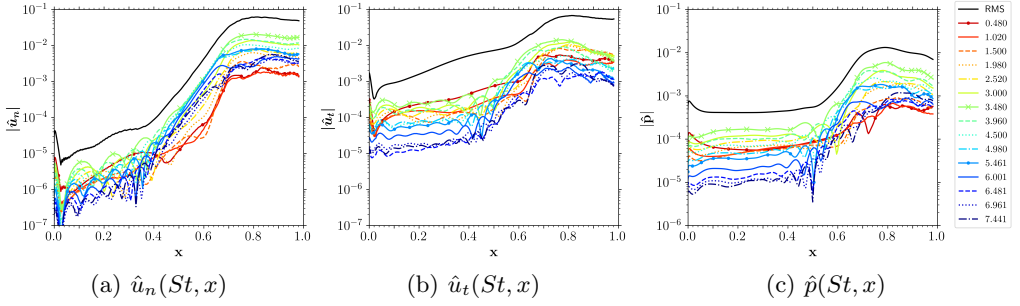


FIGURE 11. Magnitude of Fourier transform coefficients for (a) normal velocity, (b) tangential velocity and (c) pressure computed along the green (velocities) and blue (pressure) lines from figures 3(a) and (b), respectively.

computed for the spanwise averaged normal and tangential velocity components u_n and u_t , respectively, besides pressure p . Results are plotted together with the RMS values (solid black line) extracted from figure 3. Both \hat{u}_t and \hat{p} show strong amplification downstream of $x = 0.5$, which coincides with the location of the recirculation bubble. Furthermore, a plateau is observed upstream of $x = 0.5$ for pressure fluctuations, which indicates that acoustic waves dominate over hydrodynamic disturbances along this region. Pressure fluctuations at $St \approx 3.5$ exhibit higher amplitudes along the entire chord and similar observations can be made for the velocity components. As discussed by Kurelek *et al.* (2019), it is possible that these fluctuations act as a sub-harmonic forcing that stimulates the vortex merging process.

3.4. Linear analysis

Bi-global linear stability and resolvent analyses are employed to understand the most sensitive frequencies in terms of optimal forcing and response characteristics for 2D perturbations, i.e., only for spanwise wavenumber $\beta = 0$. This is justified since 2D structures are expected to radiate noise more efficiently. In the linearized NS operator, the off-diagonal terms, related to velocity gradients and shear, lead to a non-normal

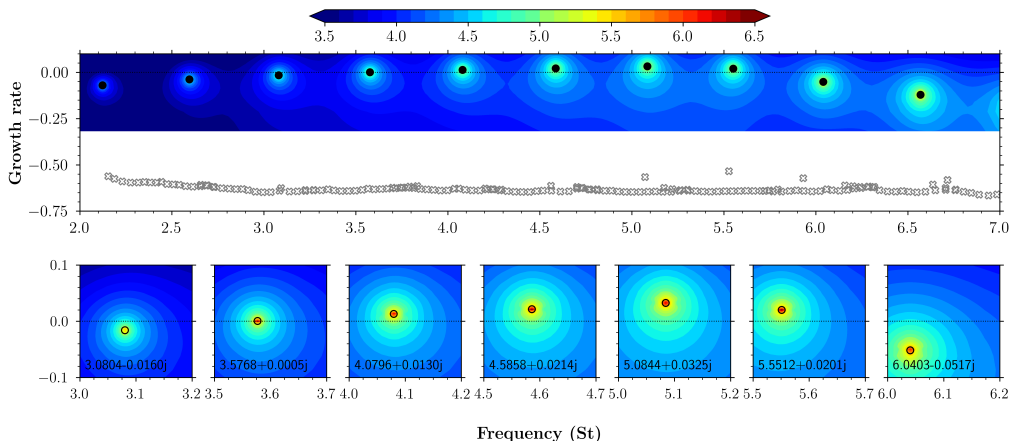


FIGURE 12. Spectrum (symbols) and pseudospectrum (contours) of the linearized compressible Navier-Stokes equations for 2D spanwise perturbations ($\beta = 0$).

operator. Hence, orthogonality of the stability modes is not expected and interaction among modes within the system may lead to transient response that affect its short-term dynamics (Schmid 2007). This behavior is properly captured by the resolvent analysis, which provides the information on eigenvalue sensitivity and transient energy amplification rate.

Following the theoretical and numerical methodology described in section 2.2, the eigenvalue spectrum from a bi-global stability analysis is presented in figure 12. The black circles represent the physically meaningful eigenvalues while the empty grey symbols are spurious eigenvalues. The latter could be identified due to their large displacement in the complex plane during the grid/sponge convergence study (not shown) as well as by visualization of the associated eigenvectors (modes). Sensitivity of the operator to external disturbances is computed by the resolvent analysis along both real (frequency) and imaginary (growth rate) axes and it is measured by the pseudospectrum, presented as the contour plot in figure 12. The region of analysis in the resolvent operator is limited by means of matrices \mathbf{B} and \mathbf{C} in equation 2.10. Only the near-field grid points are considered, i.e., those inside the dashed red rectangle in figure 1. This is physically justified since the most intense quadrupole noise sources which are responsible for the incident field in the acoustic scattering process are close to the trailing edge (Wolf *et al.* 2012a). As an additional positive side effect, this improved results by reducing spatial support of spurious eigenvectors.

Results of the spectrum in figure 12 present multiple marginally stable and unstable eigenvalues, highlighted in the magnified views in the bottom of the figure. These frequencies show promising agreement with those from the LES, presented in figures 9–11. The maximum relative deviation is less than 5%, at $St \approx 2.0$, and around 2% for the most unstable frequency $St \approx 5.0$. The pseudospectrum is shown in log-scale as a contour plot of the leading singular value from the SVD, equation 2.7. The amplification depends on both resonance and pseudoresonance (see equation 2.12) such that peaks appear when approaching an eigenvalue. The pseudoresonance levels depend on the mutual excitation of eigenvectors such that more sensitive eigenvalues present higher peaks. In this sense, figure 12 shows that higher frequencies are more sensitive compared to the lower ones. Moreover, the stable eigenvalues may impact the flow dynamics in terms of transient energy amplification given their sensitivities to disturbances.

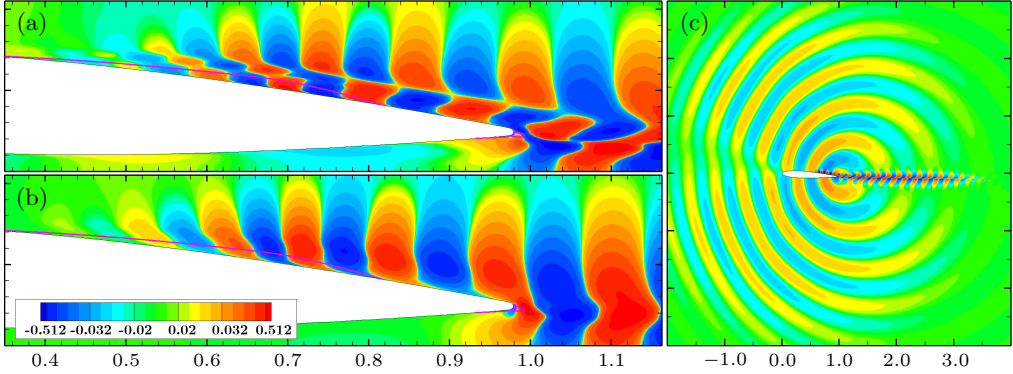


FIGURE 13. Most unstable global stability modes ($St = 5.08$) for primitive variables (a) u' , (b) v' and (c) p' .

The modal shape of each frequency is crucial to understand the system dynamics and amplification regions within the flow. In this sense, figures 13(a), (b) and (c) present the real part of the global stability modes for the most unstable frequency $St = 5.08$ in terms of u' , v' and p' , respectively. The modes are normalized with respect to the maximum value for each variable and the magnitude doubles every level to better represent lower magnitudes. The modal shapes computed for other relevant frequencies in the spectrum (resonances) show similar patterns compared to the one described here and differences are only related to the different fluctuation wavelengths. The modes displayed in the figure are related to shear layer instabilities on the airfoil suction side that lead to vortex shedding and merging in the non-linear simulation. Hence, the vortex dynamics and the multiple tones seem to be triggered by linear mechanisms. Along the separation bubble, the modal structures are tilted against the mean shear, suggesting an Orr-like mechanism for the growth of disturbances. This can be better observed by the v' fluctuations. After flow reattachment, the structures become more aligned with the wall-normal direction. The modal shapes of u' and v' display alternating positive-negative values associated with vortex-like rotational patterns. The pressure disturbances p' display upstream traveling acoustic waves radiated from the trailing edge due to scattering of vortical structures. The modes also show spatial support along the wake and, hence, wake-boundary layer coupling mechanisms cannot be discarded.

The dominant resolvent modes are computed along the neutral stability axis ($\omega_i = 0.0$) and presented in figure 14 for $St = 5.08$ in terms of kinetic energy k . The modes are normalized with respect to their maximum value. The location where disturbances are most amplified is related to the response mode. Here, the modal shape magnitude is presented such that it doubles every 2 levels. The response shows negligible amplification at the leading-edge, until the recirculation bubble. For $x > 0.4$, its magnitude increases quickly, indicating that the suction side bubble is an amplifier of disturbances. The forcing mode highlights the most receptive location, where minimal disturbances result in larger amplification by the system. This mode is related to the adjoint operator of the linearized NS equations and it is introduced in the context of airfoil secondary tones by Fosas de Pando *et al.* (2017). In the present results, the leading edge region on the suction side shows the higher values of forcing modes. Furthermore, these modes are absent in the pressure side.

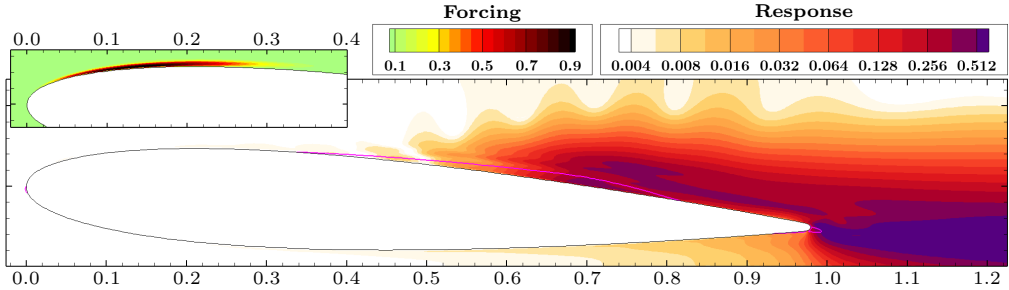


FIGURE 14. Response (white-purple contours) and forcing (upper-left plot with green-black contours) modes of kinetic energy k from the resolvent analysis along the neutral stability axis for $St = 5.08$.

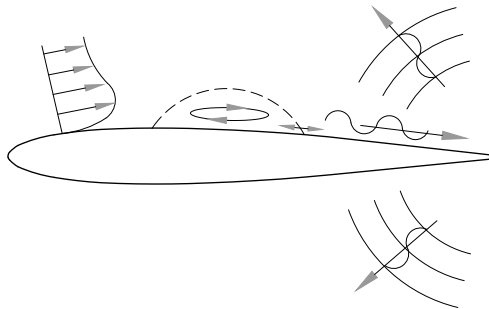


FIGURE 15. Sketch of the acoustic feedback loop.

3.5. Acoustic feedback

As discussed by several authors (Tam 1974; Lowson *et al.* 1994; Desquesnes *et al.* 2007; Jones & Sandberg 2011; Fosas de Pando *et al.* 2014b), airfoil flows at transitional Reynolds numbers are subject to an acoustic feedback mechanism that is related to the multiple tones. In this feedback process, hydrodynamic perturbations are excited in the vicinity of the leading edge and convected downstream. The disturbances amplify along the recirculation bubble on the airfoil surface and, upon reaching the trailing edge, scatter acoustic waves that travel upstream and trigger new disturbances. A sketch of this process is presented in figure 15. There are ongoing discussions about where new instabilities are generated and what is the role of the laminar separation bubble that forms along the airfoil.

The acoustic feedback mechanism fits in the resolvent analysis interpretation by McKeon & Sharma (2010) where non-linearities of the NS equations act as forcing terms, self-sustaining the flow dynamics. In this context, figures 16(a–h) present results from the resolvent analysis. In this figure, the real part of the forcing modes is shown in red-blue contours while black-white contours display the real component of the leading response modes. The yellow spots show the most receptive locations for each individual frequency. These spots in the forcing modes are shown only for regions where the magnitude reaches higher values than 98% of the maximum. As shown in figure 16, the locations of maximum receptivity change with frequency and vary along the interval $0.10 < x < 0.18$. This receptivity region is that where external actuation is more effective to disturb the flow and we conjecture that it represents the location where the acoustic feedback mechanism closes.

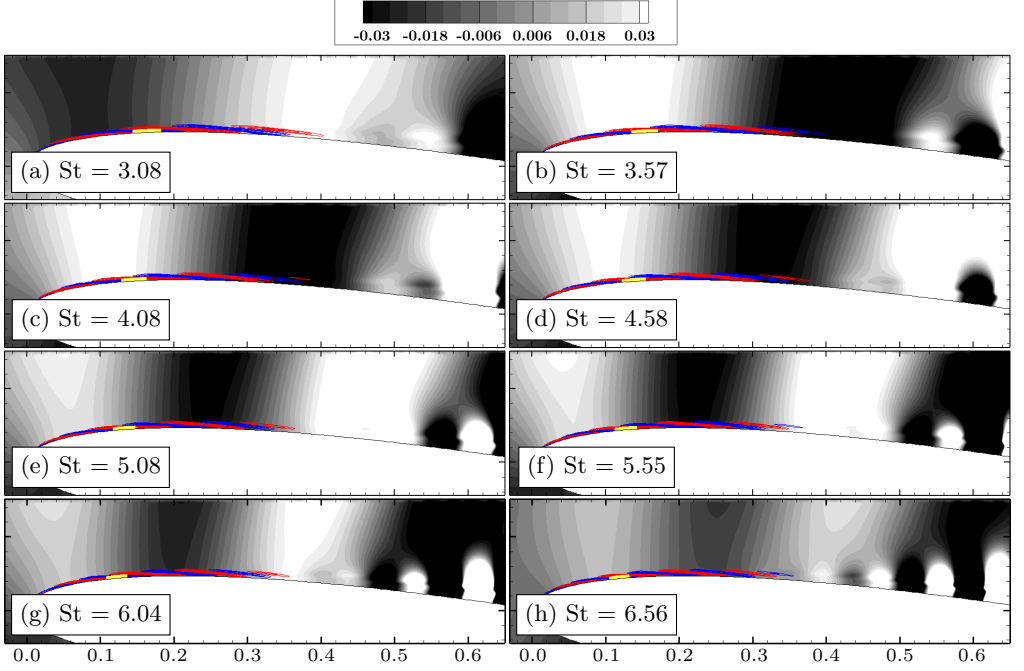


FIGURE 16. Real component of pressure response (black-white contours) and u -velocity forcing (blue-red contours) modes from resolvent analysis along the neutral stability axis. The yellow spots represent the most sensitive regions where the forcing modes achieve at least 98% of the respective maximum values for each frequency.

Aspects such as the amplitude and phase between the acoustic waves and flow receptivity at different frequencies impact the onset of hydrodynamic disturbances. To understand such complex interrelation, the acoustic feedback is analyzed using the mean flow perturbation technique to solve the linearized NS equations around the 3D mean flow in time-domain (Jones & Sandberg 2011; Fosas de Pando *et al.* 2014b). The dynamics of the pressure fluctuations is presented in figure 17. For the initial condition, a pressure disturbance is applied at the leading edge, from $x = 0.0$ to 0.005 over a short duration of $\Delta t = 1 \times 10^{-4}$ to excite all frequencies (impulse response). This triggers a wavepacket that is advected by the mean flow along the suction side. Figures 17(a,b) present the growth of disturbances for $x > 0.4$, where spatial amplification described by the response modes become important, as shown in figure 14. Figure 17(c) shows that acoustic waves are generated at the trailing edge and travel upstream. Hydrodynamic disturbances are no longer observed on the suction side after the wavepacket reaches the wake, as displayed by figure 17(d). Afterwards, disturbances in the wake slowly decay while a new wavepacket amplifies on the suction side (figures 17(e,f)). Similarly to the low frequency observed in the LES calculation, the wavepackets have a period of $\Delta t = 2.0$ and the next cycle is presented in figures 17(g–j). The combined response from the suction side wavepacket, wake instability and upstream traveling acoustic waves keeps the fluctuation field active, amplifying the globally unstable frequencies in the eigenspectrum of figure 12, which ultimately become dominant. Readers are referred to the movie provided as supplemental material (movie 4) presenting the evolution of the linearized flow dynamics.

Flow disturbances are tracked along the blue line from figure 3(b) and presented as a function of time and space in figures 18(a) and (b). The former shows pressure

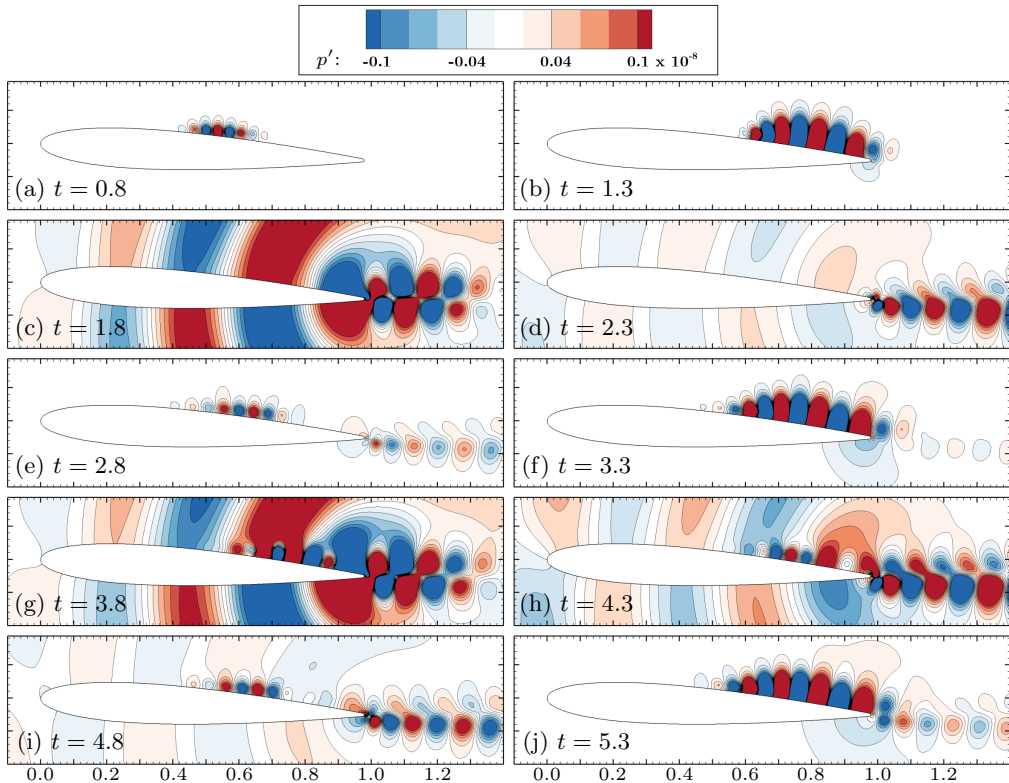


FIGURE 17. Snapshots of the linearized Navier-Stokes equations presented in terms of pressure fluctuations show periodic wavepackets composed by the multiple frequencies from the eigenspectrum of figure 12.

fluctuations p' while the latter displays disturbances of an entropy measure $(p/\rho^\gamma)'$. In these plots, the values are normalized with respect to the maximum and presented in a logarithmic scale. The positive and negative values are presented as red and blue colors, respectively. The first wavepacket shown in figures 17(a,b) is observed traveling downstream with a local mean velocity \bar{u} as bottom-up contours starting at $t = 0.0$. Upon reaching the trailing edge, at $t > 1.2$, the wavepacket generates acoustic waves propagating upstream with $\bar{u} - a$ speed. These waves are observed as top-down contours with lower magnitudes. The acoustic pressure has a phase opposition of π compared to the hydrodynamic fluctuations on the trailing edge and, hence, a negative hydrodynamic pressure fluctuation (blue) creates a positive acoustic wave (red). Upstream of $x \approx 0.4$, the acoustic waves dominate and it is not possible to see the onset of instabilities. Hence, a measure of entropy $(p/\rho^\gamma)'$ is shown in figure 18(b) to partially filter the upstream acoustic disturbances and highlight the hydrodynamic content. In this figure, the contours of hydrodynamic fluctuations from bottom-up are better visualized. In both plots, a green region covering the entire period is placed at $0.1 \leq x \leq 0.18$, illustrating the maximum forcing region from figure 16. Along this region, disturbances generated at the leading-edge ($x = 0.0$) travel downstream and appear to interact with the upstream acoustic waves. We conjecture that the simultaneous combination of acoustic and hydrodynamic forcing at this location results in the maximum response. Black lines are drawn on the plots using the convective velocity information from both pressure and entropy. These

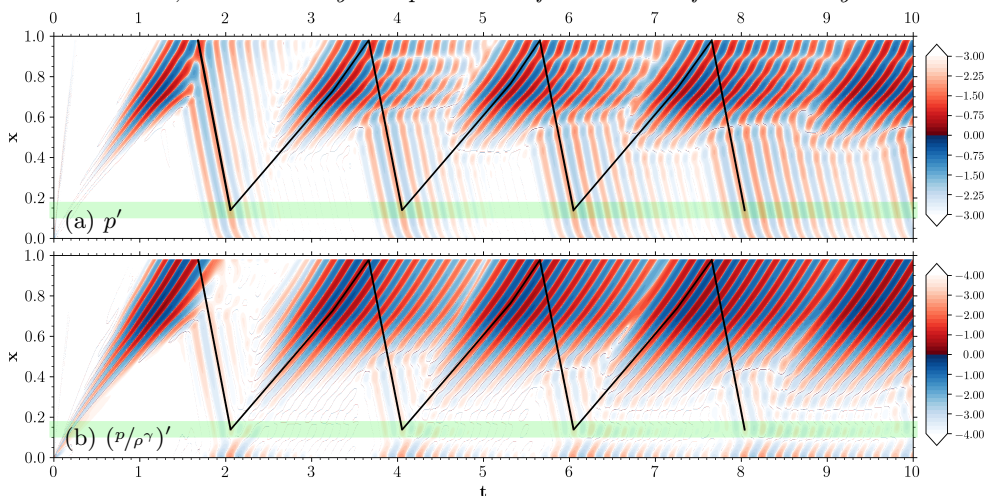


FIGURE 18. Space-time map of linear solution obtained by the mean flow perturbation for (a) pressure and (b) entropy. The map is normalized with respect to the maximum value and presented in a logarithmic scale. The positive and negative fluctuations are indicated by red and blue colors, respectively.

lines are used to track the feedback dynamics and show that, if the feedback indeed closes along the most receptive region, the period of $\Delta t = 2.0$ is satisfied.

From the computation of a real-valued pressure signal, it is possible to use the Hilbert transform to obtain its imaginary part and absolute value. The spatial shape of the wavepacket envelope is shown in figure 19(a) at the time steps indicated in figure 19(d). Its temporal evolution can be observed and the maximum value occurs at $x = 0.72$ and $t = 3.29$. The temporal signal computed at this location is presented in figure 19(b) with two envelopes. The phase information from the continuous wavelet transform of the previous signal shows in figure 19(c) that the wavepackets peak when there is phase alignment across the multiple frequencies in the eigenspectrum. Hence, constructive interference of multiple modes is crucial for maximum energy amplification. When the waves are out of phase, the wavepacket magnitude drops. The differences in phase and group velocities are presented in figure 19(d), where each curve represents a time instant indicated on the right-hand side. In this figure, the wavepacket envelopes are shown as dashed lines and their maximum locations are identified by diamond-shaped symbols. The disturbances are shown as sinusoidal-like solid lines with individual crests identified by different symbols. With this, it is possible to see that the speeds of individual disturbances are faster than the entire packet. The amplification of the latter depends on how the phase velocity of each frequency leads to phase alignment.

The feedback analysis for the non-linear LES results is performed in terms of the integral length scale obtained by the two-point correlation along the spanwise direction. Similar to the linear analysis, results are extracted along the blue line in figure 3(b). The values are normalized with respect to the maximum and results are presented in a logarithmic scale in figure 20(a) for pressure and (b) for the entropy measure. In both cases, it is possible to see high correlation values for $x > 0.4$ traveling downstream towards the trailing edge. For $x < 0.4$, smaller correlation values are presented propagating upstream towards the leading edge. Similarly to the linear analysis, the former and latter disturbances represent hydrodynamic and acoustic waves, respectively. The entropy measure partially filters the acoustic waves moving upstream. The black lines are used

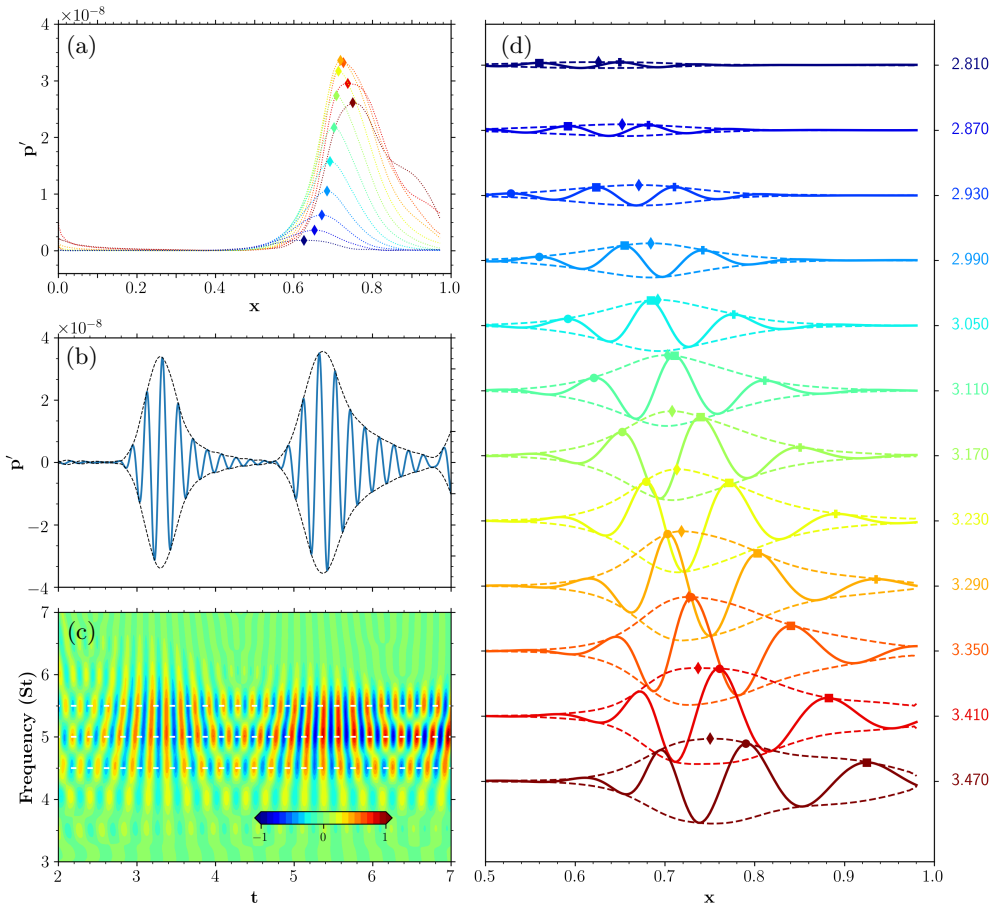


FIGURE 19. Wavepacket dynamics from linear solution including (a) spatial shape at various time instants, (b) temporal signal, (c) its phase scalogram at point of maximum amplitude and (d) spatio-temporal evolution. In the latter plot, the diamond symbol shows the maximum amplitude for each time instant and the other symbols track the wave crests.

to track disturbances assuming that the feedback mechanism takes place at $0.1 < x < 0.18$, indicated by the green shaded rectangle which represents the region of maximum receptivity from figure 16. When the acoustic waves reach this region they trigger disturbances that travel downstream. Entropy fluctuations generated at the leading edge appear to interact with the upstream-propagating acoustic waves in the region of maximum receptivity, similarly to the phenomena observed in the linear analysis.

The phase information from the LES is presented together with the spanwise pressure correlation in figures 21(a) and (b) at $x = 0.64$. This location is representative of the vortex pairing and merging region. These figures show that the high coherence depends on the phase alignment of frequencies $St \approx 4$ to 6. This frequency range corresponds to that where the most amplified modes from the linear analysis are observed. If more (fewer) frequencies are aligned, a stronger (weaker) signal coherence is achieved. If the disturbances are in phase, the result is vortex merging and strong coherence. On the other hand, if they are out of phase, the vortex pairing fails and coherence is reduced. The repeating patterns of strong correlation show that the feedback mechanism has a period of $\Delta t \approx 2.0$, related to the lower tone in the spectrum at $St = 0.5$.

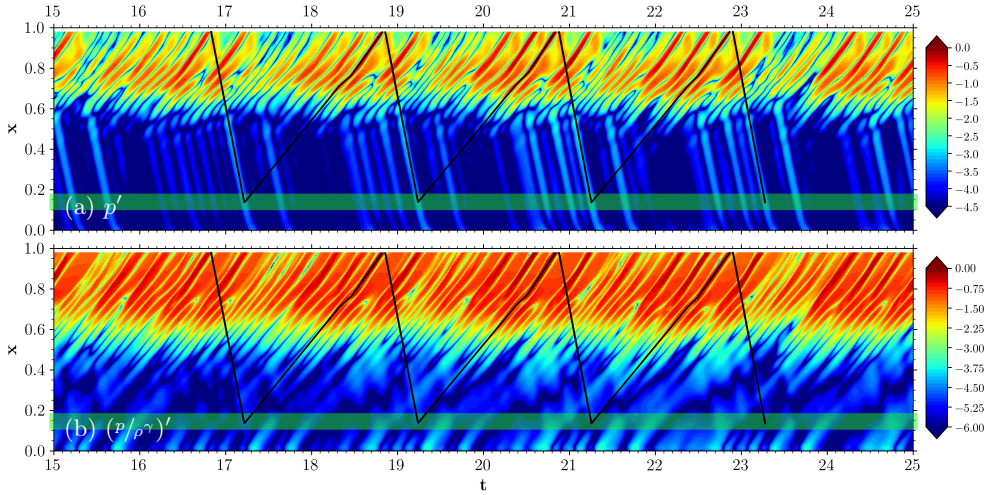


FIGURE 20. Integral length scale obtained by the two-point correlation along the spanwise direction computed as a function of chordwise position x and time t for (a) pressure and (b) entropy.

As a final remark, the repeating patterns observed in the simulations demonstrate that acoustic feedback occurs in the present flow. The present results indicate that the loop closes at the region of maximum sensitivity, downstream of the leading edge and upstream of the separation bubble. The leading edge may play an important role since, as observed from figure 20, some hydrodynamic disturbances generated in this region are also propagated and amplified by the flow, leading to strong pressure correlations at the trailing edge, independently of the acoustic feedback. These disturbances are caused by adjustment of the pressure field which is affected by variations in the airfoil circulation due to vortex shedding. It is important to mention that similar dynamics is observed in incompressible simulations with recirculation bubbles (Ehrenstein & Gallaire 2008), where acoustic waves are absent. This previous reference shows similar repeating wavepacket dynamics for a bump installed in a channel flow. Hence, the feedback mechanism may not be the only necessary condition for the occurrence of multiple tones but it still plays a role in the short-term memory of the flow. The intermittent interaction of vortex merging and bursting on the suction side may eventually disrupt the cycle altering the phase and magnitude of the tonal frequencies, and disrupting the feedback loop.

4. Conclusions

A study of trailing edge tonal noise is conducted through a combination of large eddy simulation and resolvent analysis. The focus of this investigation is on the secondary tones which arise in airfoil flows at moderate Reynolds numbers. A compressible LES is performed for the flow over a NACA 0012 airfoil at $Re = 5 \times 10^4$ and freestream Mach number $M_\infty = 0.3$. Three-dimensional effects, previously neglected in several numerical studies of airfoil multiple tones, play an important role in the flow dynamics since transition to turbulence is observed on the airfoil suction side. Despite flow transition, the noise spectrum depicts a main tone with multiple equidistant secondary tones. All tonal peaks observed are integer multiples of the lowest frequency peak.

The mean flow displays two recirculation regions, one on each side of the airfoil, where

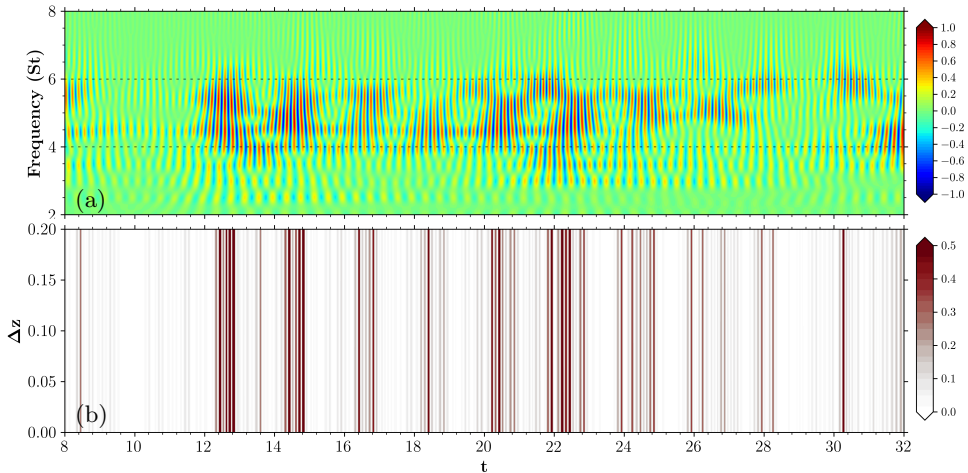


FIGURE 21. Spanwise two-point correlation dependence on constructive/destructive interference as phase aligns for frequencies $St = 4.0$ to 6.0 .

the separation bubble on the suction side is longer than that on the pressure side. The flow dynamics on the airfoil is dominated by events on the suction side, aft of the separation bubble, as indicated by the RMS values of kinetic energy and pressure. The mean friction coefficient shows a double detachment pattern, typical of large fluctuations downstream the recirculation bubble. Mean velocity profiles show that the maximum reversed velocity inside the separation bubble is 13% of the freestream value.

Vortices shed from the suction side separation bubble undergo a pairing process that may lead to either merging or bursting. As a result, coherent vortices or turbulent spots are advected towards the trailing edge. The magnitude of the radiated acoustic waves depends on the coherence level of the vortical structures, measured by two-point correlation of spanwise pressure fluctuations. The dominant tone in the sound spectrum is at the frequency in which either coherent or uncorrelated hydrodynamic structures pass by the trailing edge. On the other hand, the low frequency tone is solely related to the coherent vortices. The presence of additional highly correlated structures being transported over the trailing edge within the low frequency period impacts the magnitude of the secondary tones. This is displayed in a time-frequency analysis using continuous wavelet transforms, where the frequencies exhibit intermittent behavior with the possibility of changing the instantaneous dominant tonal frequency.

Linear stability analysis of the mean flow using a bi-global operator shows marginally stable and unstable frequencies close to those observed in the non-linear simulation, indicating that the overall flow dynamics originates from linear mechanisms. Results from resolvent analysis of the linear operator are displayed as the pseudospectrum, showing that the higher frequencies are more susceptible to be excited by pseudoresonances. The response modes show that the suction side recirculation bubble acts as an amplifier of disturbances. On the other hand, the forcing modes show a high sensitivity region within the flow, starting downstream of the leading edge and extending until upstream the bubble. In the large eddy simulation, the amplification of fluctuations along the laminar separation bubble ultimately leads to vortex shedding on the suction side. The phase alignment among these frequencies impacts the success of vortex pairing and merging aft of the bubble. This process moves the dominant tonal peak to a lower frequency than that observed in the linear spectrum.

The time integration of the linearized Navier-Stokes is performed with the mean flow

perturbation technique. The system response to an impulsive actuation at the leading edge displays a wavepacket advected towards the trailing edge with subsequent radiation of acoustic waves due to a scattering mechanism. The wavepacket is composed of multiple frequencies in the eigenspectrum and its magnitude is maximum when their phase aligns. The periodic alignment of the multiple frequencies corresponds to the low-frequency tonal peak observed in the non-linear results. Upon reaching the leading edge region, new disturbances are excited, resulting in the acoustin feedback loop mechanism discussed in literature. It is conjectured that the feedback loop closes at the most sensitive region, described by the forcing modes, in order to satisfy the low frequency motion of the wavepacket. However, this mechanism does not seem to be the only necessary condition for the multiple tones since similar dynamics is also reported for incompressible flows.

The spanwise correlation is analyzed along the airfoil chord and shows an influence of the feedback mechanism, where specific patterns repeat in time. Intermittency due to transition to turbulence may shift the phase and magnitude of all frequencies, disrupting the feedback loop. Despite this, the flow reaches a new equilibrium and reestablish the periodic merging/bursting process, indicating that the periodicity of multiple stability modes may be the self-sustaining mechanism for multiple tones and flow transition.

5. Acknowledgements

T.R. and W.W. acknowledge Fundação de Amparo à Pesquisa do Estado de São Paulo, FAPESP, for supporting the present work under research grants No. 2013/08293-7, 2018/11835-0 and 2019/20437-0, and 2019/18809-7, and Conselho Nacional de Desenvolvimento Científico e Tecnológico, CNPq, for supporting this research under grants No. 407842/2018-7 and 304335/2018-5. K.T. thanks the support from the US Office of Naval Research under grant N00014-19-1-2460. The authors thank CENAPAD-SP (Project 551), UCLA cluster Hoffman2 and LNCC-Cluster SDumont (Project SimTurb) for providing the computational resources used in this study. We also thank Prof. C.-A. Yeh, Dr. C. Skene and Mr. J. H. M. Ribeiro for insightful discussions on stability and resolvent analyses.

REFERENCES

- ARBEY, H. & BATAILLE, J. 1983 Noise generated by airfoil profiles placed in a uniform laminar flow. *J. Fluid Mech.* **134**, 33–47.
- BEAM, R. & WARMING, R. 1978 An implicit factored scheme for the compressible Navier-Stokes equations. *AIAA J.* **16** (4), 393–402.
- BHAUMIK, S., GAITONDE, D. V. & WAINDIM, M. 2015 Development of a Navier-Stokes-based numerical method for basic state perturbation analysis. In *53rd AIAA Aerospace Sciences Meeting, AIAA Paper 2015-1533*, pp. 1–21.
- BOFFETTA, G. & ECKE, R. E. 2012 Two-dimensional turbulence. *Annu. Rev. Fluid Mech.* **44** (1), 427–451.
- CHU, B.-T. 1965 On the energy transfer to small disturbances in fluid flow (part I). *Acta Mechanica* **1**, 215 – 234.
- DESQUESNES, G., TERRACOL, M. & SAGAUT, P. 2007 Numerical investigation of the tone noise mechanism over laminar airfoils. *J. Fluid Mech.* **591**, 155–182.
- DUCK, P. W., RUBAN, A. I., THEOFILIS, V., HEIN, S. & DALLMANN, U. 2000 On the origins of unsteadiness and three-dimensionality in a laminar separation bubble. *Philosophical Transactions of the Royal Society of London. Series A: Mathematical, Physical and Engineering Sciences* **358** (1777), 3229–3246.
- DUCOIN, A., LOISEAU, J.-CH. & ROBINET, J.-CH. 2016 Numerical investigation of the interaction between laminar to turbulent transition and the wake of an airfoil. *Eur. J. Mech. B* **57**, 231–248.

- EHRENSTEIN, U. & GALLAIRE, F. 2008 Two-dimensional global low-frequency oscillations in a separating boundary-layer flow. *Journal of Fluid Mechanics* **614**, 315–327.
- FARGE, M. 1992 Wavelet transforms and their applications to turbulence. *Annu. Rev. Fluid Mech.* **24**, 395–458.
- FINK, M. R. 1975 Prediction of airfoil tone frequencies. *J. Aircraft* **12** (2), 118–120.
- FOSAS DE PANDO, M., SCHMID, P.J. & LELE, S.K. 2014a Parametric sensitivity for large-scale aeroacoustic flows. In *Center for Turbulence Research, Proceedings of the Summer Program 2014*, pp. 1–13.
- FOSAS DE PANDO, M., SCHMID, P. J. & SIPP, D. 2014b A global analysis of tonal noise in flows around aerofoils. *J. Fluid Mech.* **754**, 5–38.
- FOSAS DE PANDO, M., SCHMID, P. J. & SIPP, D. 2017 On the receptivity of aerofoil tonal noise: an adjoint analysis. *J. Fluid Mech.* **812**, 771–791.
- JONES, L. E. & SANDBERG, R. D. 2011 Numerical analysis of tonal airfoil self-noise and acoustic feedback-loops. *Journal of Sound and Vibration* **330** (25), 6137–6152.
- JONES, L. E., SANDBERG, R. D. & SANDHAM, N. D. 2008 Direct numerical simulations of forced and unforced separation bubbles on an airfoil at incidence. *J. Fluid Mech.* **602**, 175–207.
- KURELEK, J. W., KOTSONIS, M. & YARUSEVYCH, S. 2018 Transition in a separation bubble under tonal and broadband acoustic excitation. *J. Fluid Mech.* **853**, 1–36.
- KURELEK, J. W., LAMBERT, A. R. & YARUSEVYCH, S. 2016 Coherent structures in the transition process of a laminar separation bubble. *AIAA J.* **54** (8), 2295–2309.
- KURELEK, J. W., YARUSEVYCH, S. & KOTSONIS, M. 2019 Vortex merging in a laminar separation bubble under natural and forced conditions. *Phys. Rev. Fluids* **4**.
- LELE, S. K. 1992 Compact finite difference schemes with spectral-like resolution. *J. Comput. Phys.* **103** (1), 16–42.
- LONGHOUSE, R.E. 1977 Vortex shedding noise of low tip speed, axial flow fans. *J. Sound Vib.* **53** (1), 25–46.
- LOWSON, M. V., FIDDES, S. P. & NASH, E. C. 1994 Laminar boundary layer aeroacoustic instabilities. In *32nd AIAA Aerospace Sciences Meeting and Exhibit, AIAA-Paper 94-0358*, pp. 1–10.
- LUCHINI, P. & BOTTARO, A. 2014 Adjoint equations in stability analysis. *Annu. Rev. Fluid Mech.* **46** (1), 493–517.
- MATHEW, J., LECHNER, R., FOYSI, H., SESTERHENN, J. & FRIEDRICH, R. 2003 An explicit filtering method for large eddy simulation of compressible flows. *Physics of Fluids* **15** (8), 2279–2289.
- MCKEON, B. J. & SHARMA, A. S. 2010 A critical-layer framework for turbulent pipe flow. *J. Fluid Mech.* **658**, 336–382.
- MICHELIS, T., YARUSEVYCH, S. & KOTSONIS, M. 2018 On the origin of spanwise vortex deformations in laminar separation bubbles. *J. Fluid Mech.* **841**, 81–108.
- NAGARAJAN, S., LELE, S. K. & FERZIGER, J. H. 2003 A robust high-order compact method for large eddy simulation. *J. Comput. Phys.* **191** (2), 392–419.
- NASH, E.C., LOWSON, M.V. & MCALPINE, A. 1999 Boundary-layer instability noise on aerofoils. *J. Fluid Mech.* **382**, 27–61.
- PATERSON, R.W., VOGT, P.G., FINK, M.R. & MUNCH, C.L. 1973 Vortex noise of isolated airfoils. *J. Aircraft* **10**, 296–302.
- PLOGMANN, B., HERRIG, A. & WÜRZ, W. 2013 Experimental investigations of a trailing edge noise feedback mechanism on a NACA0012 airfoil. *Exp. Fluids* **54** (5).
- PRÖBSTING, S., SCARANO, F. & MORRIS, S. C. 2015 Regimes of tonal noise on an airfoil at moderate Reynolds number. *J. Fluid Mech.* **780**, 407–438.
- PRÖBSTING, S., SERPIERI, J. & SCARANO, F. 2014 Experimental investigation of aerofoil tonal noise generation. *J. Fluid Mech.* **747**, 656–687.
- PRÖBSTING, S. & YARUSEVYCH, S. 2015 Laminar separation bubble development on an airfoil emitting tonal noise. *J. Fluid Mech.* **780**, 167–191.
- RAMOS, B. L. O., WOLF, W. R., YEH, C.-A. & TAIRA, K. 2019 Active flow control for drag reduction of a plunging airfoil under deep dynamic stall. *Phys. Rev. Fluids* **4**, 074603.
- RANJAN, R., UNNIKRISHNAN, S. & GAITONDE, D. V. 2018 On the use of mean flow perturbation for global stability analysis. In *2018 Fluid Dynamics Conference*.

- REDDY, S. C. & HENNINGSON, D. S. 1993 Energy growth in viscous channel flows. *J. Fluid Mech.* **252**, 209–238.
- RIBEIRO, J. H. M., YEH, C.-A. & TAIRA, K. 2020 Randomized resolvent analysis. *Phys. Rev. Fluids* **5**, 033902.
- RICCIARDI, T. R., ARIAS-RAMIREZ, W. & WOLF, W. R. 2020 On secondary tones arising in trailing-edge noise at moderate Reynolds numbers. *Eur. J. Mech. B* **79**, 54–66.
- RICCIARDI, T. R., RIBEIRO, J. H. M. & WOLF, W. R. 2019 Analysis of coherent structures in large-eddy simulations of a NACA0012 airfoil. In *AIAA Scitech 2019 Forum*, *AIAA Paper 2019-0320*.
- RICCIARDI, T. R., WOLF, W. R. & TAIRA, K. 2021 Compressibility effects in airfoil secondary tones. In *AIAA Scitech 2021 Forum*, *AIAA Paper 2021-0455*.
- SANJOSE, M., TOWNE, A., JAISWAL, P., MOREAU, S., LELE, S. K. & MANN, A. 2019 Modal analysis of the laminar boundary layer instability and tonal noise of an airfoil at Reynolds number 150,000. *Int. J. Aeroacoustics* **18**, 317–350.
- SCHMID, P. J. 2007 Nonmodal stability theory. *Annu. Rev. Fluid Mech.* **39** (1), 129–162.
- SCHMID, P. J. & HENNINGSON, D. S. 2001 *Stability and Transition in Shear Flows*. Springer.
- SUN, Y., TAIRA, K., CATTAFESTA, L. N. & UKEILEY, L. S. 2017 Biglobal instabilities of compressible open-cavity flows. *J. Fluid Mech.* **826**, 270–301.
- SYMON, S., ROSENBERG, K., DAWSON, S. T. M. & MCKEON, B. J. 2018 Non-normality and classification of amplification mechanisms in stability and resolvent analysis. *Phys. Rev. Fluids* **3**, 053902.
- TAIRA, KUNIHICO, BRUNTON, STEVEN L., DAWSON, SCOTT T. M., ROWLEY, CLARENCE W., COLONIUS, TIM, MCKEON, BEVERLEY J., SCHMIDT, OLIVER T., GORDEYEV, STANISLAV, THEOFILIS, VASSILIOS & UKEILEY, LAWRENCE S. 2017 Modal analysis of fluid flows: An overview. *AIAA Journal* **55** (12), 4013–4041, arXiv: <https://doi.org/10.2514/1.J056060>.
- TAIRA, KUNIHICO, HEMATI, MAZIAR S., BRUNTON, STEVEN L., SUN, YIYANG, DURAISAMY, KARTHIK, BAGHERI, SHERVIN, DAWSON, SCOTT T. M. & YEH, CHI-AN 2020 Modal analysis of fluid flows: Applications and outlook. *AIAA Journal* **58** (3), 998–1022, arXiv: <https://doi.org/10.2514/1.J058462>.
- TAM, C. K. W. 1974 Discrete tones of isolated airfoils. *J. Acoust. Soc. Am.* **55** (6), 1173–1177.
- TOUBER, E. & SANDHAM, N. D. 2009 Large-eddy simulation of low-frequency unsteadiness in a turbulent shock-induced separation bubble. *Theoretical and Computational Fluid Dynamics* **23** (2), 79–107.
- TREFETHEN, LLOYD N., TREFETHEN, ANNE E., REDDY, SATISH C. & DRISCOLL, TOBIN A. 1993 Hydrodynamic stability without eigenvalues. *Science* **261** (5121), 578–584, arXiv: <https://science.sciencemag.org/content/261/5121/578.full.pdf>.
- WOLF, W. R., AZEVEDO, J. L. F. & LELE, S. K. 2012a Convective effects and the role of quadrupole sources for aerofoil aeroacoustics. *J. Fluid Mech.* **708**, 502–538.
- WOLF, W. R., AZEVEDO, J. L. F. & LELE, S. K. 2013 Effects of mean flow convection, quadrupole sources and vortex shedding on airfoil overall sound pressure level. *J. Sound Vib.* **332**, 6905–6912.
- WOLF, W. R., LELE, S. K., JOTHIPRASARD, G. & CHEUNG, L. 2012b Investigation of noise generated by a DU96 airfoil. In *18th AIAA/CEAS Aeroacoustics Conference (33th AIAA Aeroacoustics Conference)*, *AIAA Paper 2012-2055*, pp. 1–15.
- YEH, C.-A. & TAIRA, K. 2019 Resolvent-analysis-based design of airfoil separation control. *J. Fluid Mech.* **867**, 572–610.